Title

Parietal top-down projections balance flexibility and stability in adaptive learning

Authors

Eunji Jung[1,4], Jong-Hoon Lee[2,3,4], Gil-Hyun Kim[3], Geonhui Ryu[1], Seung-Hee Lee[1,2,3,*]

Affiliations

[1]Department of Biological Sciences, Korea Advanced Institute of Science and Technology, 291 Daehak-ro, Yuseong-gu, Daejeon, 34141, Republic of Korea

[2]KAIST Institute for the BioCentury, Korea Advanced Institute of Science and Technology, 291 Daehak-ro, Yuseong-gu, Daejeon, 34141, Republic of Korea

[3]Center for Synaptic Brain Dysfunctions, Institute for Basic Science, Daejeon 34141, Republic of Korea

[4]These authors contributed equally.

*Corresponding author: shlee1@kaist.ac.kr

Abstract

The ability to flexibly modify behavior in response to changing environmental contingencies is fundamental to adaptive decision-making, yet how distributed brain circuits coordinate such rapid adaptation remains unclear. Here, we show that the posterior parietal cortex (PPC) facilitates adaptive learning via parallel projections to the auditory cortex (AC) and inferior colliculus (IC). In a within-session auditory reversal task, AC neurons supported flexible stimulus updating following rule reversal, whereas IC neurons preserved stable auditory discrimination across rules. Dual retrograde tracing revealed anatomically segregated PPC neurons projecting to AC (PPC_{AC}) and IC (PPC_{IC}). PPC_{AC} neurons flexibly encoded stimulus-outcome contingencies, while PPC_{IC} neurons stably represented response outcomes. Circuit-specific optogenetic inactivation confirmed their distinct contributions to behavioral adaptation. This double dissociation reveals a circuit mechanism by which parallel PPC projections coordinate flexible rule updating and stable motor execution, enabling rapid behavioral adaptation and providing a mechanistic framework for cognitive flexibility.

Introduction

Behavioral flexibility, the ability to adapt behavioral responses to changes in environmental contexts even under the same stimulus condition, depends on the capacity to flexibly associate sensory information with appropriate motor responses[1,2]. While the fronto-parietal network (FPN) has traditionally been considered central to behavioral flexibility[3-5] by actively updating task information for the re-mapping of stimulus-outcome associations[6-8], sensory areas also dynamically adjust their representations based on task-relevant contingencies[9-11]. This modulation of sensory representation is critical for animals to flexibly adapt their behaviors by prioritizing the most relevant stimuli[12-14]. Reversal learning tasks, which require updating behavioral responses following reversed stimulus-outcome contingencies, provide a powerful paradigm for measuring behavioral flexibility[2,15]. During reversal learning, the frontal cortex exhibits increased activity during rule updating[16], while the sensory cortex shows activity changes after complete behavioral reversal[17,18]. However, the functional role of top-down projections, potentially from the FPN to sensory areas, during contingency reversal remains unclear.

The posterior parietal cortex (PPC), with its extensive bidirectional connections to both sensory areas and the frontal cortex[19,20], is well-positioned as a potential mediator of behavioral flexibility during reversal learning[21,22]. In flexible learning tasks, the PPC not only encodes task-relevant stimuli[23] but also enhances the representation of task-relevant sensory information in the sensory cortex through its top-down projections[24,25]. Additionally, it retains the history of behavioral contingencies, allowing it to guide future decisions[26,27]. These functions suggest that the PPC acts as a flexible hub capable of updating outcome contingencies during reversal learning. However, whether the PPC provides top-down feedback to sensory areas specifically during reversal learning, updating stimulus contingencies and improving the

53 encoding of relevant stimuli remains unknown.

54 Auditory areas, such as the auditory cortex (AC) and inferior colliculus (IC), display
55 flexibility in representing auditory stimuli depending on task demands. AC neurons modulate
56 their auditory responses based on task rules during flexible rule-switching[17,28] and show
57 adaptive tuning to new auditory boundaries during re-categorization tasks[12]. Similarly, the IC
58 exhibits modulations in its auditory responses influenced by internal states, such as
59 locomotion[29] and attention[30]. Moreover, both the AC and IC encode task-relevant non-sensory
60 information, including action- and reward-related signals[17,31-39]. Such representational changes
61 and the integration of non-sensory information suggest the involvement of higher cortical
62 regions that project to these sensory areas and exert top-down modulation[18,21,40,41]. The circuit
63 mechanisms underlying the parallel top-down modulation of both the AC and IC during
64 reversal learning have yet to be explored.

65 In this study, we show that parallel top-down projections from the PPC to the AC and
66 IC enable flexible adaptation during within-session auditory Go/No-go reversal learning. AC
67 flexibly updated auditory representations after reversal learning, while IC stably encoded
68 auditory stimuli. Consistently, pharmacological inactivation of the AC impaired the ability to
69 adapt to reversed stimulus-outcome contingencies, whereas silencing the IC disrupted auditory
70 discriminability irrespective of contingency. We further identified anatomically segregated
71 PPC subpopulations projecting to AC (PPC_{AC}) and IC (PPC_{IC}) by dual retrograde tracing.
72 Projection-specific calcium imaging and optogenetic perturbations demonstrated that PPC_{AC}
73 flexibly updates stimulus-outcome associations, while PPC_{IC} maintains stable reward-
74 associated responses by encoding behavioral outcomes during reversal learning. These findings
75 reveal a circuit-level division of labor within the PPC, balancing flexibility and stability to
76 support rapid behavioral adaptation.

Result

Fast transition of behavioral responses in mice performing a within-session auditory reversal learning task

To assess the behavioral flexibility of mice in rapidly adapting to reversed stimulus-outcome contingencies, we developed a within-session auditory reversal learning task for head-fixed mice using a Go/No-go paradigm (Fig. 1a; Methods). Initially, mice were trained to discriminate between two pure tones of different frequencies under the first rule (R1). In this phase, they learned to lick in response to a low-frequency tone (Go, 5kHz) to receive a water reward and to withhold licking after hearing a high-frequency tone (No-go, 10kHz). Once mice achieved expert-level performance (correct response rate exceeding 0.75 within 200 trials), the task was switched to the second rule (R2) in which the stimulus-outcome contingencies were reversed (Go, 10 kHz; No-go, 5 kHz) within the same session. On the first day of the reversal learning task, mice exhibited high false alarm (FA) rates in R2, as they continued licking to the previously rewarded but now reversed No-go stimulus (5 kHz), while showing low Hit rates for the newly assigned Go stimulus (10 kHz). However, after several days of training, they learned to adjust more quickly, rapidly adapting their licking behavior to align with the new contingencies within a single session (Fig. 1b; Extended Data Fig. 1a-b). Training continued until mice consistently achieved a performance rate exceeding 0.75 across both rules (Extended Data Fig. 1a).

To quantify how quickly mice learned the reversed rule, we measured the trial-number-to-reversal (TTR), defined as the number of trials required to reach stable performance in R2 (Methods). Across training sessions, correct rates in R2 gradually enhanced, ultimately reaching expert-level performance (0.837 ± 0.016 correct rate), while TTRs progressively decreased, indicating improved reversal learning over time (Extended

Data Fig. 1c). Expert mice exhibited an average TTR of 28.5 ± 13.88 trials (Extended Data Fig. 1d). Notably, lick reaction times were slightly increased in R2 compared to R1 (Extended Data Fig. 1e), while overall lick rates remained consistent across rules (Extended Data Fig. 1f).

Differential contributions of the AC and IC during auditory reversal learning

To determine whether auditory representations adapt to the reversed contingencies during reversal learning, we recorded single-unit activity from the AC (n = 400) and IC (n = 179) using linear silicon probes (three mice per region, with two recorded in both; Fig. 1c and Supplementary Table 1). Behavioral performance of mice, including performance rates, TTRs, reaction times, and lick rates, did not differ significantly between the two recording groups (Extended Data Fig. 1g-k; Supplementary Table 1).

We first examined whether neurons that were selective for stimulus identity during R1 maintained their selectivity in R2. We calculated a 5kHz vs. 10kHz tone selectivity index (SI) for individual neurons using receiver operating characteristic (ROC) analysis[18,23] based on their firing rates in each rule, where +1 indicates a preference for 5kHz and -1 for 10kHz (Methods). We then compared SI values across rules to assess changes in selectivity after contingency reversal. Based on these comparisons, we classified neurons into five categories (Fig. 1d): stably selective (auditory tone selective, green), contingency updated (Go or No-go selective, light blue), and neurons that lost (yellow) or gained (red) selectivity. Compared to IC neurons, a significantly larger proportion of AC neurons exhibited flexible changes in stimulus selectivity (either by shifting stimulus preference according to contingency or by gaining/losing selectivity across rules; AC, n = 151 of 240; IC, n = 58 of

115; Fig. 1e-g), indicating that stimulus representations in the AC are more flexibly changed than those in the IC following reversal.

We next evaluated changes in stimulus selectivity from R1 to R2 by calculating the difference in SIs (Δ SI) for individual neurons and comparing their distributions in AC and IC using kernel-density estimation. AC neurons exhibited a more positive shift in ΔSI compared to IC neurons, indicating enhanced selectivity (i.e., improved discrimination of Go/No-go stimuli) following rule reversal (Fig. 1h, i). These results reveal distinct dynamics of stimulus selectivity across sensory areas during auditory reversal learning: the AC shows greater flexibility and enhanced discriminability for task-relevant auditory stimuli after contingency reversal, whereas the IC maintains more stable representations.

To examine the causal roles of auditory sensory areas in rapid adaptation during auditory reversal learning, we inactivated the AC and IC using muscimol (MUS), a $GABA_A$ receptor agonist, in expert mice performing the task (Fig. 2a; Extended Data Fig. 2 and Supplementary Table 2; Methods). Bilateral AC inactivation impaired auditory reversal learning in mice, as indicated by increased TTRs, reduced Hit rates, and elevated FA rates in R2, while leaving performance in R1 unaffected (Fig. 2b-e; Extended Data Fig. 2b, e, f). In contrast, unilateral IC inactivation disrupted auditory discrimination performance of mice both in R1 and R2, significantly reducing Hit rates in both phases (Fig. 2f, g; Extended Data Fig. 2c, g, h). Control PBS injections had no effect on behavior in both AC and IC (Fig. 2b-g; Extended Data Fig. 2b, c, e-h). These results indicate a functional dissociation and complementary roles of distinct auditory areas during auditory reversal learning, with the AC supporting behavioral flexibility following a rule reversal, and the IC ensuring performance stability by maintaining consistent auditory discrimination and reliable execution of learned responses across task phases.

148

149 **PPC sends top-down projections to AC and IC and is critical for auditory reversal**
150 **learning**

151 To identify potential top-down inputs modulating auditory responses in the AC and IC,
152 we performed dual-color retrograde tracing by injecting retrograde adeno-associated viruses
153 (AAVrg) expressing GFP and tdTomato into the AC and IC, respectively (Fig. 3a). Whole-brain
154 clearing and light-sheet microscopy revealed distinct anatomical projections to both structures
155 (Fig. 3b, c; Supplementary Movie 1, 2). The orbitofrontal cortex (OFC), secondary motor
156 cortex (M2), and cingulate cortex area 1 (Cg1) predominantly projected to the AC (Fig. $3c_{i\text{-}ii}$),
157 while the medial prefrontal cortex, including prelimbic (PrL) and infralimbic (IL) cortex, and
158 cingulate cortex area 2 (Cg2) primarily innervated the IC (Fig. $3c_{i\text{-}ii}$; Supplementary Movie 2).
159 The insular cortex (InC), extending from the anterior to the posterior axis, mainly projected to
160 the IC, whereas the adjacent claustrum (Cl) exhibited strong projections to the AC (Fig. $3c_{ii\text{-}iii}$).

161 Unlike other brain regions that selectively projected to either the AC or IC, both the
162 PPC and temporal association cortex (TeA), corresponding to the dorsal and ventral association
163 cortices, respectively, contained two anatomically distinct and topographically segregated
164 populations labeled with GFP and tdTomato (Fig. 3b, c_{iv}; Supplementary Movie 1, 2). In
165 particular, we observed robust dual labeling in the PPC, indicating that this region provides
166 parallel top-down inputs to both the AC and IC (Fig. 3b, d, e). Within the PPC, neurons
167 projecting to the IC (PPC_{IC}) accounted for approximately 19.30 % (± 4.69%) of total labeled
168 cells, while those projecting to the AC (PPC_{AC}) comprised 82.03 % (± 4.61%) (Extended Data
169 Fig. 3). Neurons co-labeled with both tracers were rare, constituting only 1.66 % (± 0.31%)
170 and 7.85% (± 1.93%) of the labeled PPC_{AC} and PPC_{IC} neurons, respectively. Notably, PPC_{AC}
171 neurons were distributed along the mediolateral axis, with a higher density in the lateral PPC

172 (PPC-L), whereas PPC_{IC} neurons were predominantly located in the medial PPC (PPC-M) (Fig.
173 3b, e). Relative depth measurements from the pia mater to the ventricle using 4′,6-diamidino-
174 2-phenylindole (DAPI)-stained sections (Fig. 3d; Methods) further revealed that PPC_{AC}
175 neurons were distributed across multiple cortical layers, from superficial to deep, whereas
176 PPC_{IC} neurons were primarily restricted to deep layers (Fig. 3e). These anatomical distinctions
177 are consistent with previously reported features of intratelencephalic (IT) and pyramidal tract
178 (PT) cortical neuron subtypes[42,43].

179 To further investigate the role of the PPC in auditory reversal learning, we bilaterally
180 inactivated this region in behaving mice using MUS injections. Similar to the effects observed
181 with AC inactivation (Fig. 2b-e; Extended Data Fig. 2b, e, f), PPC inactivation resulted in a
182 significant increase in TTRs after the rule switch, along with reductions in both Hit rates and
183 overall correct rates (Fig. 3f-i; Extended Data Fig. 2d, i, j). Importantly, this impairment was
184 specific to reversal learning, as auditory discrimination performance during R1 remained
185 unaffected (Fig. 3f, h; Extended Data Fig. 2d, i, j). Control experiments using PBS injections
186 showed no changes in TTRs or task performance (Fig. 3g, i; Extended Data Fig. 2d, i, j),
187 confirming that the observed deficits were specifically attributable to PPC inactivation. These
188 findings demonstrate the critical role of the PPC in auditory reversal learning by enabling mice
189 to flexibly adapt to new stimulus-outcome contingencies following a rule switch.

190

191 **PPC_{AC} exhibits flexible reorganization of population activity, while PPC_{IC} remains stable,**
192 **during reversal learning**

193 Given the distinct functional modulations observed in the AC and IC during reversal
194 learning (Fig. 1, 2), along with the anatomically segregated PPC projections to these regions
195 (Fig. 3), we hypothesized that parallel PPC top-down circuits may differentially update

196 reversed contingencies to shape the distinct contributions of the AC and IC to adaptive behavior.
197 To address this, we performed projection-specific *in vivo* calcium (Ca^{2+}) imaging using
198 transgenic mice expressing GCaMP6f under the control of Cre recombinase (Ai148). We
199 selectively labeled PPC neurons projecting to either the AC or IC by injecting AAVrg vectors
200 expressing Cre recombinase into each area and measured their Ca^{2+} activity in mice performing
201 the auditory reversal learning task (Fig. 4a, b; Methods). A total of 283 PPC_{AC} neurons and 111
202 PPC_{IC} neurons showed sufficient activity for analysis. Behavioral performance measures,
203 including correct rates, TTRs, lick rates, lick reaction times, and lick rates across rules and trial
204 types, were similar between the PPC_{AC} and PPC_{IC} imaging groups (Extended Data Fig. 4a-e;
205 Supplementary Table 3).

206 To visualize the temporal dynamics of population activity across rules, we applied
207 Rastermap, a scaled k-means clustering algorithm[44,45], to neuronal activity during R1 and
208 plotted the cluster-ordered activity across R1, transition (TR; early R2 up to the TTR), and
209 post-transition R2. While PPC_{IC} neurons maintained similar activity patterns across rules,
210 PPC_{AC} neurons exhibited marked reorganization (Fig. 4c, d; Extended Data Fig. 4f, g). To
211 further characterize these population-level dynamics, we performed principal component
212 analysis (PCA; Methods) and projected population activity trajectories of Go and No-go trials
213 from R1, TR, and R2 onto a common PC space (Fig. 4e, f). Both PPC_{AC} and PPC_{IC} populations
214 showed distinct representations of Go and No-go contingencies across rules, but Go trajectories
215 were more pronounced in PPC_{IC} neurons. Notably, PPC_{AC} trajectories displayed flexible
216 remapping across rules, with dual divergence for both trial types and rules (Fig. 4e), whereas
217 PPC_{IC} trajectories remained largely stable, showing minimal shifts following the rule reversal
218 (Fig. 4f).

219 To quantify these differences, we calculated subspace overlaps of population activity

220 across task phases (Fig. 4g; Extended Data Fig. 4h, i; Methods). Both PPC_{AC} and PPC_{IC}
221 populations exhibited strong within-rule overlaps, reflecting consistent activity during stable
222 contingencies. However, PPC_{AC} neurons showed a significant reduction in overlap during the
223 TR phase, indicating dynamic reorganization of their activity during contingency updating. In
224 contrast, PPC_{IC} neurons maintained stable subspace overlaps across all phases and exhibited
225 significantly higher across-rule overlaps than PPC_{AC} neurons, reflecting preserved and strong
226 encoding of Go contingencies across rules (Fig. 4h, i). Together, these results suggest that
227 PPC_{AC} neurons flexibly reorganize their activity to incorporate new stimulus-outcome
228 relationships, whereas PPC_{IC} neurons sustain stable representations of reward-associated
229 contingencies, potentially supporting consistent behavioral responses following rule reversal.

230

231 **PPC top-down projections encode distinct task variables during reversal transition**

232 Given the differential network dynamics of PPC_{AC} and PPC_{IC} neurons during the TR
233 phase, we next investigated how these populations contribute to behavioral adaptation
234 following contingency reversal. We applied a generalized linear model (GLM; Methods) to
235 assess how individual neurons encoded task variables (TVs) that require updating during TR.
236 These TVs included stimulus identity (5kHz or 10kHz tones), behavioral outcomes (Hit, FA,
237 Correct Rejection (CR), and Miss), and motor responses (lick-bout onset and offset) (Fig. 5a-
238 e). Overall, 55% of PPC_{AC} neurons (156/283) and 50% of PPC_{IC} neurons (55/111) significantly
239 encoded at least one TV, with PPC_{IC} neurons exhibiting a stronger overall model fit compared
240 to PPC_{AC} neurons (Fig. 5b, c).

241 We further analyzed the fraction of TV-encoding neurons (Fig. 5d) and their temporal
242 dynamics across the trial epoch (Fig. 5e-o). We found distinct encoding patterns between the

two PPC output pathways. A greater fraction of PPC_{AC} neurons encoded auditory stimuli compared to PPC_{IC} neurons (Fig. 5d-f, l), whereas PPC_{IC} neurons showed stronger encoding of licking responses (Fig. 5d, e, g, m). Both populations robustly encoded lick-associated outcomes (Hit and FA) (Fig. 5d, e, h, i, n, o), but only PPC_{AC} neurons strongly represented outcomes associated with the absence of licking (CR and Miss) (Fig. 5d, e, j, k; Extended Data Fig. 5a, b). Furthermore, PPC_{AC} neurons exhibited more distributed and prolonged outcome encoding throughout the trial period (Fig. 5h-k; Extended Data Fig. 5c, d), whereas PPC_{IC} neurons primarily encoded lick-related outcomes restricted to the response window (Fig. 5n, o; Extended Data Fig. 5e). Notably, GLM analysis during the R1 and R2 phases revealed that both populations encoded fewer TVs in these more stable stages: PPC_{AC} neurons primarily encoded stimuli, Hit outcomes, and licking onset, while PPC_{IC} neurons encoded only Hit outcomes and licking onset (Extended Data Fig. 5f-i). These results suggest that PPC neurons increase their encoding of task-relevant outcomes specifically during the reversal transition, supporting their role in updating stimulus contingencies during reversal learning.

Interestingly, PPC_{AC} neurons tended to encode a greater number of TVs per neuron compared to PPC_{IC} neurons, although this difference did not reach statistical significance (Fig. 5p, s; PPC_{AC}: 2.61 ± 1.18, PPC_{IC}: 2.18 ± 0.92, Kolmogorov-Smirnov test, $p = 0.19$). Multiplexed encoding analysis further revealed that PPC_{AC} neurons exhibited more distributed co-encoding across multiple TVs (Fig. 5p), whereas PPC_{IC} neurons were predominantly tuned to Hit, FA, and lick-related variables (Fig. 5s). In PPC_{IC}, neurons encoding lick events showed greater overlap with those encoding Hit or FA outcomes compared to PPC_{AC}, but both groups exhibited weaker overlap between lick-encoding and CR- or Miss-encoding neurons (Fig. 5q, t). This overlapping pattern suggests that outcome-related activity in PPC_{IC} during the transition phase may be more strongly modulated by changes in licking behavior. Finally,

267 10kHz- and 5kHz-encoding neurons in PPC_{AC} were largely non-overlapping and not
268 selectively associated with any specific outcomes or motor variables (Fig. 5r), indicating that
269 auditory information is likely processed by a distinct subnetwork within PPC_{AC}. Together, these
270 results demonstrate that PPC_{AC} neurons flexibly and dynamically encode newly relevant
271 stimulus-outcome contingencies, whereas PPC_{IC} neurons maintain stable encoding of lick-
272 related outcomes during contingency reversal.

273

274 **Double dissociation of top-down projections from the PPC during reversal learning**

275 Given the distinct encoding properties of PPC_{AC} and PPC_{IC} neurons during auditory
276 reversal learning, we investigated the functional roles of these two top-down pathways in
277 task execution. To selectively manipulate each circuit, we optogenetically inactivated
278 PPC_{AC} or PPC_{IC} neurons by retrogradely labeling them with archaerhodopsin (ArchT)
279 through bilateral injections of AAVrg expressing ArchT under the CaMKIIa promoter into
280 the AC or IC, respectively (Fig. 6a, b; Supplementary Table 4). Each projection was
281 selectively inhibited using green laser light, either during the initial trials following the rule
282 reversal (40-80 trials including the TR phase; Type I inactivation) or in randomly selected
283 trials during stable task phases (R1 or R2; Type II inactivation). In both conditions, laser
284 light was delivered from -1 s before stimulus onset through the response window.

285 Type I inactivation of PPC_{AC} neurons led to perseverative errors, evidenced by a
286 decrease in Hit rates, an increase in FA rates, and an increase in TTRs (Fig. 6c-f), suggesting
287 a failure to update reversed stimulus-outcome contingencies. Conversely, inactivation of
288 PPC_{IC} neurons resulted in an overall reduction in licking during R2, with a prominent
289 reduction of Hit rates, indicating an inability to maintain licking responses after the rule

290 reversal (Fig. 6g-j). Control mice expressing eYFP in the PPC showed no behavioral
291 alterations under the same stimulation protocol (Extended Data Fig. 6), confirming the
292 specificity of the effects to projection-specific inactivation. In contrast, Type II inactivation
293 had no effect on performance, regardless of whether light was applied during the stimulus
294 period (Fig. 6k-r). These findings suggest that neither PPC_{AC} nor PPC_{IC} activity is required
295 for stable auditory discrimination once the task contingencies are established. Instead, both
296 pathways are specifically required behavioral adaptation during contingency reversal.

297 Collectively, our results reveal a double dissociation between PPC_{AC} and PPC_{IC}
298 function in reversal learning. PPC_{AC} inactivation impairs contingency updating, leading to
299 perseverative licking responses to previously rewarded but now No-go stimuli. PPC_{IC}
300 inactivation, however, disrupts execution of Go responses, reflecting a failure to maintain
301 licking responses after the rule change. These functional dissociations align with the distinct
302 TV-encoding properties of each population, highlighting that parallel PPC top-down circuits
303 play distinct but complementary roles in guiding flexible behavioral adaptation.

Discussion

Behavioral flexibility is essential for survival in dynamic environments, requiring the brain to flexibly adapt to changing rules while maintaining stable, goal-directed behavior. Previous studies have highlighted the roles of prefrontal and parietal regions in flexible reversal learning and executive control[2,46,47], yet the circuit-level mechanisms balancing flexibility and stability in mammalian brains remain unclear. Here, we identify a novel organizational principle in the mouse brain, where anatomically segregated top-down projections from the PPC to AC and IC serve complementary roles in behavioral adaptation during auditory reversal learning. PPC projections to AC (PPC_{AC}) dynamically reorganize their activity to encode stimulus-outcome contingencies, supporting flexible rule updating. In contrast, projections to IC (PPC_{IC}) stably represent lick-associated outcomes across rules and are specifically engaged during response execution. Both projections are necessary for successful reversal learning: inactivating PPC_{AC} impairs contingency updating, whereas silencing PPC_{IC} disrupts stable behavioral execution. This double dissociation demonstrates how parallel PPC circuits coordinate flexible updating of internal models with stable execution of learned behaviors.

The architecture of the PPC suggests a generalized top-down circuit motif for balancing flexibility and stability. By anatomically segregating its outputs, the PPC may minimize interference between adaptive and stable computations, thereby reducing the risk of degraded learning performance. This dual-output strategy addresses a fundamental challenge in cognitive systems: integrating new information without erasing previously learned associations[48]. While this issue, known as catastrophic forgetting, is well documented in artificial neural networks[49], biological reversal learning typically involves gradual adaptation, allowing old memory and new learning to coexist[50-53]. In our study, mice continued to lick in response to auditory cues, potentially supported by stable PPC-to-IC circuit, while gradually

adapting to reversed stimulus-outcome contingencies via flexible PPC-to-AC circuit. Thus, projection-specific segregation in the PPC may serve to buffer against interference and promote cognitive flexibility through distributed top-down control.

Moreover, our findings broaden the functional roles of the AC and IC beyond auditory processing, revealing distinct contributions during auditory reversal learning. Similar to previous reports[14,32,37], we observed the AC is not required for stable discrimination before reversal, but its activity is necessary for flexible adaptation after rule reversal. In contrast, the IC activity is required for behavioral responses to reward-associated cues across phases. These results align with emerging evidence that the IC integrates auditory and motor signals to coordinate sensory input with goal-directed behavior[36,38,54-57]. Extending this view, our data show that PPC-to-IC projections convey motor-outcome signals directly to the IC. Unlike the more flexible cortico-cortical PPC-to-AC pathway, this projection may enhance behavioral efficiency by facilitating rapid and reliable responses to reward-predicted stimuli. Such a mechanism may reflect an evolutionarily conserved strategy that supports fast action execution to optimize reward acquisition for survival. Future studies are required to clarify how non-sensory PPC top-down signals interact with auditory processing in AC and IC neurons to guide adaptive behavior during contingency reversal.

Methods

Animals

All experimental procedures were approved by the KAIST Institutional Animal Care and Use Committee (IACUC-18-100, IACUC-18-235). Animals were housed under controlled environmental conditions with a 12-hour light/dark cycle (8 am - 8 pm / 8 pm - 8 am) and provided *ad libitum* access to food and water. Throughout the experimental period, mice were individually housed at a controlled temperature (20 - 22°C) and humidity (30 to 50%). We used C57BL/6 wild-type mice and B6.Cg-Igs7tm148.1(tetO-GCaMP6f, CAG-tTA2)Hze/J mice (Ai148, Jackson Laboratory, stock no. 030328) of both male and female, aged 2-6 months. Detailed information regarding the number of animals used in each experimental condition is provided in the corresponding figure legends and supplementary data tables.

Surgery

Common procedure for animal surgery

Adult mice (P45-P80) were anesthetized with 1.5-2% isoflurane in oxygen, and their heads were fixed in a stereotaxic apparatus using ear bars. Body temperature was maintained at 37°C using a feedback-controlled heating pad (CWE Inc.). Following hair removal, the scalp was sterilized with 70% ethanol and povidone-iodine solution. A midline incision was made using surgical scissors for virus injection, or a portion of the scalp was removed for head plate implantation. After removing the periosteum above the skull, the exposed skull surface was cleaned with 70% ethanol, povidone-iodine solution, and sterile filtered phosphate-buffered saline.

Virus injection for dual-color retrograde tracing

For dual-color retrograde tracing, we injected ~ 0.5 μl of retrograde adeno-associated virus (AAVrg) expressing tdTomato (pAAV-CAG-tdTomato, Cat# 59462-AAVrg, Addgene) and eGFP (pAAV-CAG-GFP, Cat# 37825-AAVrg, Addgene) into the right AC (posterior 2.5 mm and lateral 4.2 mm from bregma; depth 0.7 mm) and the right IC (posterior 5.2 mm and lateral 0.8 mm from bregma; depth 0.8 mm), respectively, of a wild-type mouse using a KDS Legato 130 Syringe Pump (RWD) at a rate of 0.3nl/sec. After 14 ~ 15 days post-injection, brain samples were collected for histological analysis following transcardial perfusion.

Head plate implantation surgery for mouse head-fixation

For head plate implantation, mice were prepared as described above, including scalp incision and removal of connective tissues. We marked the PPC (posterior + 1.95 mm and lateral 1.4~1.6 mm from bregma; depth 0.4 mm), AC, and IC for subsequent pharmacological inactivation experiments, *in vivo* extracellular recordings, and optogenetic manipulations. For lens implantation, a 1 mm × 1 mm area was demarcated on the skull 0.2 mm away from the PPC target coordinates. The custom-designed head plate was securely attached to the skull using a combination of small screws (Small Parts), cyanoacrylate glue (Loctite super glue 401, Henkel), and dental cement (Super-Bond C&B Kit, Sun Medical Co.). Following surgery, mice were closely monitored for their health status, and behavioral training began after a minimum recovery period of one week.

Surgical procedures for in vivo Ca^{2+} imaging with a miniature microscope

For circuit-specific Ca^{2+} imaging, ~0.5 µl of AAVrg-hsyn-cre (pENN.AAV.hSyn.Cre.WPRE.hGH, Cat# 105553-AAVrg, Addgene) was injected into either the AC or IC of the right hemisphere in Ai148 mice before head-plate mounting. The exposed brain tissue at the injection site was covered with cured Kwik-Sil (WPI). Following a 7 - 10 day viral incubation period, mice began water restriction for behavioral training. During training on the auditory reversal learning task (see Methods; Behavior), mice had full access to water until they returned to their baseline weight, ensuring proper health before the subsequent lens implantation surgery.

Gradient refractive index (GRIN) lens implantation was performed following established protocols[58]. Mice received subcutaneous injections of carprofen (5 mg/kg) and dexamethasone (5 mg/kg) at least 1 hour before surgery. Under anesthesia, a 1 mm × 1 mm craniotomy was made 0.2-0.3 mm anterior to the target field of view (FOV: PPC_{AC}, AP -1.65 mm; PPC_{IC}, AP -1.45 mm). The craniotomy location accounted for the working distance of the miniature microscope. A small linear incision was made in the cortical surface using a surgical knife (Cat# 10055-12, Fine Science Tools,) at the planned lens insertion site. The prism-attached GRIN lens (Cat# 1050-004624, Inscopix) was slowly inserted at a rate of 0.1 mm/20 s to a depth of 0.9-1.0 mm along the medio-lateral axis. The exposed brain tissue between the GRIN lens and skull was sealed with cured Kwik-Sil, followed by Super-Bond application to secure the lens. To protect the GRIN lens surface from debris during the recovery period, Kwik-Sil was applied to the top of the lens. Post-operative care included subcutaneous carprofen and dexamethasone injections for three consecutive days to manage pain and inflammation. After a 2-week recovery, water restriction was reinstated to resume behavioral training. Once mice regained stable performance (>0.75 correct rate) in the auditory reversal task, the FOV for each

413 mouse was examined for clear detection of neuronal activity. Following confirmation of a
414 suitable imaging quality of FOV, a baseplate (Cat# 1050-004683, Inscopix) was attached to the
415 GRIN lens using dental acrylic (Ortho-Jet, Lang Dental) and Super-Bond, then secured with a
416 baseplate cover (Cat# 1050-004639, Inscopix).

417

418 *Surgical procedure for optogenetic manipulation in task-performing mice*

419 For circuit-specific optogenetic manipulations, AAVrg-CaMKII-ArchT (pAAV-
420 CamKII-ArchT-GFP, Cat# 99039-AAVrg, Addgene) was bilaterally injected into the AC or IC
421 of wild-type mice in the test group. Control animals were injected with AAV2-CaMKII-eYFP
422 (UNC) bilaterally. All viral injections were performed on the same day prior to head-plate
423 implantation. After a 7 - 10 day period for virus expression, mice began water restriction for
424 behavioral training. Once mice reached expert performance in the auditory reversal learning
425 task (see Methods; Behavior), they were provided unrestricted water access for at least 2 days
426 to prepare for optic fiber implantation. Under anesthesia with 1.5 ~ 2 % isoflurane, bilateral
427 craniotomies (~0.5 mm diameter) were made over the PPC using either manual drilling or a
428 biopsy punch (Cat# 12-460-414, Fisher scientific, manufacturer). Optic fibers (200 μm core
429 diameter, Cat# FT200UMT, Thorlabs) with ferrules (CFLC230-10, Thorlabs) were implanted
430 into the PPC at a depth of 0.35mm and secured with Kwik-Sil (WPI) and Super-Bond.
431 Following a 2-day recovery period, water restriction was resumed for optogenetic manipulation
432 experiments.

433

434 **Behavior assay**

Hardware setup

Auditory stimuli were digitally generated using custom MATLAB code (sampling rate 192,000 Hz, 16bit) with 5 ms sinusoidal ramps at stimulus onset and offset. A speaker (Ultrasonic Dynamic Speaker Vifa, Avisoft-Bioacoustics) was positioned 10 ~ 12cm from the head-fixation apparatus. The sound pressure level (SPL) of both stimuli was calibrated to 75dB using a Reference Signal Generator and an externally polarized condenser microphone (CM16/CMPA, Avisoft-Bioacoustics), positioned at the same distance as the mouse's left ear relative to the speaker. A custom-built lickometer was used to detect individual licking events during the task. Both outcomes (water reward and air puff punishment) were delivered through separate solenoid valves (EV-2-24, Clippard). All hardware components were controlled by Presentation (Neurobehavioral Systems) using a USB data acquisition board (USB-201, Measurement Computing).

Behavior training for the auditory reversal learning task

Before behavioral training, mice underwent initial water deprivation until their body weight dropped below 80% of their pre-deprivation weight, typically after three days of deprivation. Body weight was monitored daily and maintained above 75% of the initial weight throughout the water restriction period. During behavioral experiments, mice were kept on ~1 ml of water per day to ensure consistent performance. Task performance was evaluated based on Hit rate, False Alarm (FA) rate, and Correct rate, which were calculated as follows:

(1) Hit rate = $\frac{\#\ of\ Hit\ trials}{\#\ of\ Go\ trials}$

(2) FA rate = $\frac{\#\ of\ FA\ trials}{\#\ of\ No-go\ trials}$

(3) Correct rate = $\frac{\#\ of\ Hit\ trials + \#\ of\ Correct\ Rejection\ trials}{\#\ of\ Go\ trials + \#\ of\ No{-}go\ trials}$

To assess perceptual flexibility in mice, we adapted and modified a reversal learning task from previous research[23,59]. The task consisted of five stages:

1. Reward conditioning stage: Water-restricted mice received 1μl of water upon licking the water port. If mice did not initiate licking behavior within 3 minutes from the session start, water was manually delivered through the port until voluntary licking was established. Mice progressed to the next stage if they achieved more than 1,000 licks within 20 minutes.

2. R1 conditioning stage: Mice were trained to discriminate between Go (5kHz) and No-go (10kHz) pure tones (500 ms duration), presented pseudo-randomly in a 1:1 ratio. A 2-second response window followed a 500 ms delay after stimulus presentation. During Go trials, licking within the response window (Hit) triggered a 3 μl water reward and a 2-second consumption period. If mice did not lick (Miss trials), water was automatically delivered after the response window to encourage the Go stimulus-reward association. No-go trials had no consequences with licking (FA) or not licking (CR). The session included a 4-second inter-trial interval and terminated after 20 consecutive Miss trials. Mice advanced to the next stage if they achieved a Hit rate above 0.8.

3. R1 learning stage: Mice were trained to discriminate between 5 kHz and 10 kHz tones in a Go/No-go paradigm with reward and punishment. The paradigm was similar to the conditioning stage, except for two critical differences: no water reward for Miss trials and negative outcomes for FA trials (4 - 8s timeout and/or 100 - 800 ms air puff).
4. Reversal learning task with conditioning stage: Once mice reached a ≥0.75 correct rate in the initial rule (R1), they proceeded to the reversal learning stage, where the Go/No-

go contingencies were reversed within a single session. To facilitate the rule transition, classical conditioning (CS) trials were introduced immediately following the reversal, during which a reward was delivered after Go stimuli regardless of licking behavior. CS trials were progressively reduced in 20-trial increments once mice achieved ≥0.75 correct rates for both R1 and R2. When the number of CS trials reached 40, the delay period was extended from 500 ms to 1,000 ms. Mice exhibiting persistent cross-rule impulsive licking were returned to R1 training. Task performance during CS trials was evaluated based on anticipatory licking behavior[59], with licks during the delay period classified as Hits or FAs depending on the stimulus contingency. All subsequent experiments, including electrophysiology, drug treatments (MUS and PBS), Ca^{2+} imaging and optogenetics were conducted at this stage.

5. Reversal learning expert stage: Mice that demonstrated a ≥0.75 correct rate for at least three consecutive days in the R2 stage (without CS trials) were classified as reversal experts. Subsequent experiments, including drug treatments, Ca^{2+} imaging, and optogenetics were conducted at this stage.

Quantification of trial-number-to-reversal (TTR) and transition (TR) phase

To quantify the speed of adaptation to reversed contingencies (R2), we defined a metric termed trial-number-to-reversal (TTR). Following rule reversal, a 10-trial moving average of binary choice accuracy (Correct = 1, Incorrect = 0) was computed. TTR was defined as the final trial in the first sequence of three consecutive trials where this moving average exceeded 0.7. The TR phase was defined as the period between the contingency reversal and TTR (Fig. 1). In sessions that included CS trials, TTR was calculated using both CS and standard trials, with anticipatory licking responses used to assess response accuracy.

Pharmacological inactivation

To investigate the role of specific brain regions in auditory reversal learning, we performed local neural inactivation through bilateral microinjections of either the $GABA_A$ receptor agonist muscimol (MUS, 1 μg/μl; Sigma-Aldrich) or 1X PBS (control) into PPC, AC, and IC. Each hemisphere received 0.23 μl of solution. Behavioral testing in the auditory reversal task commenced 20 minutes post-injection to ensure adequate drug diffusion and effect. To control for individual variability and enable within-subject comparisons, mice were tested across multiple sessions in the following sequence: pre-injection baseline (no injection; Pre), muscimol injection (MUS), and PBS injection. Fluoro-ruby (Cat# AG335, Sigma-Aldrich) was injected with PBS to verify the injection site by histology. For specific subgroups (AC, N=1; IC, N=3; PPC, N=2), performance measures were averaged across sessions to generate a single data point per animal.

Optogenetic manipulations

For circuit-specific optogenetic inactivation during the reversal task, AAVrg-CaMKIIa-ArchT-GFP was bilaterally injected into either the AC (PPC_{AC}) or IC (PPC_{IC}), followed by bilateral optical fiber implantation in the PPC. To probe the temporal specificity of PPC inputs during behavioral adaptation, we employed two laser stimulation protocols (Type I and II inactivation):

1. Type I: Continuous green laser stimulation (532 nm, 10-12 mW) from 1 s before stimulus onset to the end of the response window (trial epoch).

2. Type II (Control): Trial-epoch stimulation delivered in pseudo-randomly selected trials.

For Type I, the number of stimulated trials was set by rounding up the TTR measured during matched laser-off sessions (up to a maximum of 80 trials) to ensure coverage of the TR phase. Type II served as controls to confirm that observed effects were specific to the transition stage.

In vivo **electrophysiological recordings**

Neural activity recording during task

Neural recordings from AC and IC in task-performing mice were conducted using a 64-channel probe (P64-12, Diagnostic Biochips. Inc.). A 1 mm diameter craniotomy was made one day prior to recording and covered with an artificial dura-like material (Duragel, Cambridge Neurotech) to protect the exposed brain tissue. For each animal, 3 to 5 recording tracks were made in each target area. Neural data were acquired using an OpenEphys data acquisition board and software at 30kHz, with an amplifier gain of 192 for each channel. Signals were bandpass filtered with cutoff frequencies at 300 Hz and 6000 Hz. To confirm the recording sites and perform post hoc histological analysis, electrodes were coated with lipophilic dye (1,1'- dioctadecyl-3,3,303'- tetramethylindocarbocyanine perchlorate (DiI), Invitrogen) before insertion.

Spike sorting for single-unit isolation

Spike sorting was performed using an automated spike-sorting MATLAB toolbox Kilosort to cluster units from raw data[60]. The resulting spike clusters were manually curated

using Phy (Kwik team). Further quality control was conducted with custom MATLAB codes to ensure high-quality single-unit data. A total of 579 single units were recorded from AC and IC in 4 animals.

Selectivity index

The selectivity of each neuron to stimulus identity was quantified using ROC analysis, as previously described[23,61]. This analysis was conducted separately for R1 and R2 by comparing time-averaged firing rate changes in response to 5kHz stimulus and 10kHz stimulus across trials. We captured both increased and suppressed neuronal responses by quantifying the absolute changes in firing rates (|Δfiring rates|) during the stimulus period (0 to 500 ms) relative to the pre-stimulus period (-500 to 0 ms) in each trial. We excluded trials with licking events detected close to the stimulus period (from - 500 to + 750 ms from the stimulus onset) to minimize any contamination of motor-related activity. Stimulus selectivity (SI) was then computed for each neuron from the area under the ROC curve (AUC) as follows:

(4) $SI = (AUC - 0.5) \times 2$

SI value of +1 indicates that the firing rate changes were always higher in response to 5kHz tone compared to 10kHz tone, while -1 indicates 10kHz preference. Statistical significance of the SI was assessed by a permutation test across trials (1,000 iterations, $p < 0.05$). Neurons were classified into five types based on their SI values in R1 vs. R2: none (not significant across rules), stimulus (significantly selective to the same stimulus across rules), lost (became non-significant after rule reversal), acquired (became significant after rule reversal), and contingency (significantly selective to the reversed stimuli across rules

570 following associated outcome). To plot firing rate changes in representative neuronal types,
571 peri-stimulus time histograms (PSTHs) of spike trains for 5kHz and 10kHz stimuli in R1
572 and R2 were generated separately by averaging trial-by-trial firing rates in 10-ms bins and
573 smoothing with a Gaussian kernel ($\sigma = 50$ ms).

574

575 **Circuit-specific Ca^{2+} imaging and data analysis**

576 *Data acquisition and processing*

577 We performed *in vivo* Ca^{2+} imaging using a miniature fluorescence microscope and
578 the nVista 3.0 data acquisition system (Inscopix)[62,63] with LED power of 0.2~ 0.4 mW and a
579 gain value of 1 ~ 4, collecting data at 20 frames per second.

580 Data processing was performed using Inscopix Data Processing Software (IDPS). The
581 preprocessing pipeline included spatial down-sampling (by 4), spatial filtering, and motion
582 correction to mitigate motion artifacts. We used Constrained Non-negative Matrix
583 Factorization for micro-endoscopic data (CNMF-E) to identify regions of interest (ROIs)
584 corresponding to individual cells. ROI detection was configured with a cell diameter between
585 5 to 7 pixels and standard thresholds for minimum pixel correlation (0.60 to 0.80) and minimum
586 peak-to-noise ratio (8.00 to 10.00) to ensure Ca^2 signal detection while minimizing false
587 positives. After automated ROI detection, we manually curated the results to match
588 fluorescence traces ($\Delta F/F_0$) with ROIs and eliminate contamination from out-of-focus neuropil
589 fluorescence. To correct for fluorophore photo-bleaching, we applied a correction method from
590 a previously published protocol[64], using the following equation:

591 (5) $F_{corrected(t)} = F_{subt(t)} - G_{(t)} + < F_{subt(t)} >_t$

This equation calculated the corrected fluorescence signal ($F_{corrected(t)}$) by subtracting slow baseline fluctuations averaged over a 300-second sliding window ($G_{(t)}$) and adding back the overall mean fluorescence across the recording session ($\langle F_{sub(t)} \rangle_t$).

Rastermap visualization

To visualize task-related Ca^{2+} activity, we applied Rastermap[44,45], a k-means clustering-based sorting algorithm that highlights temporally correlated patterns in neural population activity. Among the tunable parameters, we selected a cluster number of 50 for sorting population activity. Importantly, choosing alternative values (e.g., 25 or 100 clusters) did not alter the overall patterns or conclusions of our observations (Extended Data Fig. 6a, b).

Principal Component Analysis (PCA)

Ca^{2+} activity was averaged for each trial type and task phase, then concatenated to form a $6T \times N$ matrix, where T represents the duration of each trial segment (2 second pre-stimulus onset and 6 seconds post-stimulus onset) and N is the number of imaged neurons. We then performed principal component analysis (PCA) using *scikit-learn* (Python library). Neural trajectories were computed by projecting the data onto the first three principal components (PCs). Out of 798 recorded neurons (594 PPC_{AC} neurons and 194 PPC_{IC} neurons), we selected neurons with an average $\Delta F/F_0$ greater than 0.05 (283 PPC_{AC} neurons and 111 PPC_{IC} neurons) to reduce noise introduced during Ca^{2+} trace normalization for PCA. Importantly, using the full set of imaged neurons yielded similar results.

Subspace overlap analysis

Normalized Ca^{2+} traces were trial-averaged in 50-trial segments S_i (i = 1, ... 7) across R1 (S1-S3; 1 to 150 trials), TR (S4; R2 to TTR + 15 trials) and R2 (S5-S8; 1 to 150 trials post S4). We then performed PCA to compute low-dimensional neural subspaces for each segment. To quantify subspace overlap, we calculated the cosine of the principal angle between each pair of subspaces, as previously published[65]. The principal angle (θ_p) between two subspaces *U* and *V* corresponds to the largest angle between any two pairs of vectors in *U* and *V*, providing a measure of their alignment. For each segment S_i, we extracted the first N principal components and organized them into an N × N matrix **R** (S_i), defining the subspace of that segment. The cosine of the principal angle between subspaces S_i and S_j was computed using the method described by Knyazev and Argentati[66], as follows:

$$(6)\quad \cos\theta_p(s_i, s_i) = \sigma_{max}(R(s_i)^T R(s_j))$$

where $\sigma_{max}(A)$ denotes the largest singular value of matrix A.

Generalized linear models (GLM)

We used generalized linear models (GLM) to regress recorded Ca^{2+} signals against task event variables[64,67,68]. Ca^{2+} responses for each neuron were modeled as a linear sum of task components and events, including lick-bout onset and offset, Go stimulus (10kHz) and No-go stimulus (5kHz), Hit, FA, CR, and Miss.

The neural response at time t ($\hat{y}_t$) was modeled by the sum of the bias term (β_0) and the weighted sum of various binary predictors (x_i) as follows:

$$(7)\ \hat{y}_t = \beta_0 + \sum_{i=0}^{10} \beta_i^{Go} x_i^{Go} + \sum_{i=0}^{10} \beta_i^{Nogo} x_i^{Nogo} + \sum_{i=0}^{60} \beta_i^{Hit} x_i^{Hit} + \sum_{i=0}^{60} \beta_i^{FA} x_i^{FA}$$

$$+ \sum_{i=0}^{60} \beta_i^{Miss} x_i^{Miss} + \sum_{i=0}^{60} \beta_i^{CR} x_i^{CR} + \sum_{i=-5}^{10} \beta_i^{lon} x_i^{lon} + \sum_{i=-5}^{10} \beta_i^{loff} x_i^{loff}$$

Predictors for each task variable were convolved with temporal filters to capture the slow dynamics of Ca^{2+} signals[69]. Predictors for Go (x_i^{Go}) and No-go (x_i^{Nogo}) stimuli indicated stimulus presence, while lick predictors represented onset (x_i^{lon}) and offset (x_i^{loff}) of lick bouts, defined as sequences with inter-lick intervals of less than 2 seconds. Predictors for behavioral outcomes, including Hit (x_i^{Hit}), FA (x_i^{FA}), CR (x_i^{CR}), miss (x_i^{Miss}), included time lags to cover the duration of stimulus presentation, reward consumption, and slow Ca^{2+} dynamics. Time lags were set to 0-1 second for stimulus predictors, 0-6 seconds for outcome predictors, and -0.5 to 1 second for lick-related predictors, where 0 denotes the event onset time. The full model contained up to 321 coefficients, including the bias term (β_0).

To avoid overfitting, we used a bottom-up approach. First, initial single-variable models were fitted for each neuron using *ElasticNet* linear regression with combined ridge (L1) and lasso (L2) regularization from the scikit-learn Python library. Models were cross-validated twenty-fold, using 30% of total trials for validation. The task variable with the highest average R^2 score significantly above 0 (Student's t-test) was selected. If no task variable was selected, the neuron was considered not fitted by the GLM. Coefficients for additional task variables were added iteratively, comparing goodness of fit until no further improvement was observed. The regularization parameter α was optimized over a wide range of values (1×10^{-5} to 10) to maximize performance.

To visualize patterns of neuronal multiplexing, defined as co-encoding of two or more

task variables, we first identified all unique combinations of co-encoded variables. Each multiplexing pattern was ranked by frequency to determine the most common pairings. For neurons encoding more than two task variables, all possible pairwise combinations were counted individually. For example, if a neuron encoded "Hit," "FA," and "CR" simultaneously, it contributed one count to each of the following pairs: “Hit-FA”, “Hit-CR”, and “FA-CR”. This approach enabled us to quantify how frequently each pair of task variables was co-encoded across the population. To visualize these relationships, we used a circular Sankey diagram, in which curved connections between task variables represent co-encoding patterns, with line thickness proportional to the frequency of co-occurrence.

Histology and imaging

Fluorescence imaging of brain sections

Histological experiments were conducted to verify anatomical circuit tracings, confirm targeting sites after pharmacological inactivation, identify electrode tracks following *in vivo* recordings, and validate optogenetic manipulation and Ca^{2+} imaging sites. Mice were deeply anesthetized with isoflurane and intraperitoneal injection of avertin (2,2,2,-Tribromoethanol; 125-250 mg/kg; Sigma-Aldrich), and transcardially perfused with 10ml of phosphate-buffered saline (PBS) followed by 4% paraformaldehyde (wt/vol in 1X PBS). Brain samples were carefully extracted and post-fixed for 4 hours at room temperature, then washed 3 times in 1X PBS for 10 minutes each. The samples were transferred to a filtered 30% sucrose solution (wt/vol in 1X PBS) and allowed to sink completely for 1~2 days at 4°C. Brain samples were embedded in the optimal cutting temperature (OCT) compound (Tissue-Tek, Sakura Finetek),

679 rapidly frozen at -80°C, and coronally sectioned at 30 μm (for tracing) or 40 μm (for site
680 verification) using a cryostat (Leica). Sections were washed three times in 1X PBS for 10
681 minutes to remove residual OCT medium. The sections were mounted on glass slides with a
682 mounting medium containing 4′,6-diamidino-2-phenylindole (DAPI, Vector Labs) for nuclear
683 staining and tissue visualization. Fluorescent images were acquired using a slide scanner (Axio
684 Scan Z1, Carl Zeiss).

685

686 *Tracing analysis*

687 For dual-retrograde tracing analysis, three coronal brain sections (30 μm thick) were
688 collected from each of three mice. Sections were selected based on stereotaxic coordinates from
689 the Paxinos atlas (AP -1.70 mm, -1.84 mm, and -2.06 mm from the bregma). Using IMARIS
690 software (Oxford Instruments), brain section images were aligned to the reference atlas, and
691 anatomical boundaries were matched to delineate the PPC, including its medial (PPC-M) and
692 lateral (PPC-L) subdivisions. Labeled cells within these boundaries were detected using the
693 IMARIS Cell Detection function, with DAPI colocalization used to confirm accurate cell
694 identification. The spatial coordinates (x, y, z) of verified cells were exported for custom
695 MATLAB-based analysis. To assess layer-specific distributions, atlas boundaries were
696 imported into IMARIS to guide selection of DAPI signals corresponding to pia and ventricular
697 surfaces. Cortical depth was normalized by regression fitting of DAPI signals along these
698 boundaries, with the pia-to-ventricle distance scaled to a depth of 1. This normalization allowed
699 direct comparison of relative laminar distributions between PPC_{AC} and PPC_{IC} populations.

700

701 *Whole-brain clearing and 3D imaging*

Whole-brain clearing was performed using the Binaree Tissue-Clearing Kit (HRTC-012 and HRMO-006, Binaree, Inc.) following a previously published protocol[70]. After perfusion and brain extraction, the tissue-clearing process proceeded as follows: The brain was incubated in a starting solution at 4°C for 24 hours. The brain was then transferred to tissue-clearing solutions and incubated at 37°C with 50 rpm agitation for 48 hours. This clearing step was repeated to achieve complete tissue transparency. The brain was rinsed three times in a washing solution, then incubated in a mounting and storage solution at 37°C for 24 hours. For imaging, a Lightsheet 7 fluorescence microscope (Carl Zeiss) was used to acquire z-stack images of the cleared brain. The resulting images were reconstructed in 3D using IMARIS software.

Statistical analysis

Data analysis was conducted using Microsoft Excel, custom MATLAB (MathWorks) and Python scripts. All data are presented as means ± standard error of the mean (SEM) unless otherwise specified. 'N' denotes the number of mice, while 'n' represents the number of sessions or neurons. Statistical differences were evaluated through repeated measures two-way ANOVA, Wilcoxon signed-rank test (non-parametric, paired datasets), Paired t-test (parametric, paired datasets), Wilcoxon rank-sum test (non-parametric, unpaired datasets), two-sided chi-square test (non-parametric, frequency counts), Mood's median test (non-parametric, unpaired datasets), Sign-test (non-parametric, zero median of single population), and Two-sample Kolmogorov-Smirnov test. All the statistical significances are indicated as *, **, ***, **** for $p < 0.05$, $p < 0.01$, $p < 0.001$, and $p < 0.0001$, respectively.

Acknowledgments

This work has been supported by grants to S.H.L. from the Institute for Basic Science (IBS-R002-A2).

Author Contributions

E.J. and S.L. conceptualized and initiated the project. E.J., J.L., and S.L. designed experiments and wrote the manuscript. E.J. and J.L. jointly performed data analysis and visualization. E.J. performed behavioral training, histology, Ca^{2+} imaging, optogenetic experiments, and some *in vivo* recordings. J.L. established *in vivo* electrophysiology recordings and implemented subspace overlap and GLM analyses. G.R. conducted some *in vivo* recordings and behavioral training. G.K. performed brain clearing and cell detection.

Data and code availability

Source data are provided with this paper. All the representative data and code that support the findings are publicly available on GitHub: https://github.com/seungheelee1789/PPC_RL_Jung_Lee. Further requests for the data generated in this study can be directed to the corresponding author (shlee1@kaist.ac.kr).

Ethics declarations

Competing interests

The authors declare no competing financial interests.

Figures and figure captions

Fig. 1. Distinct auditory response modulations of the AC and IC during within-session auditory reversal learning

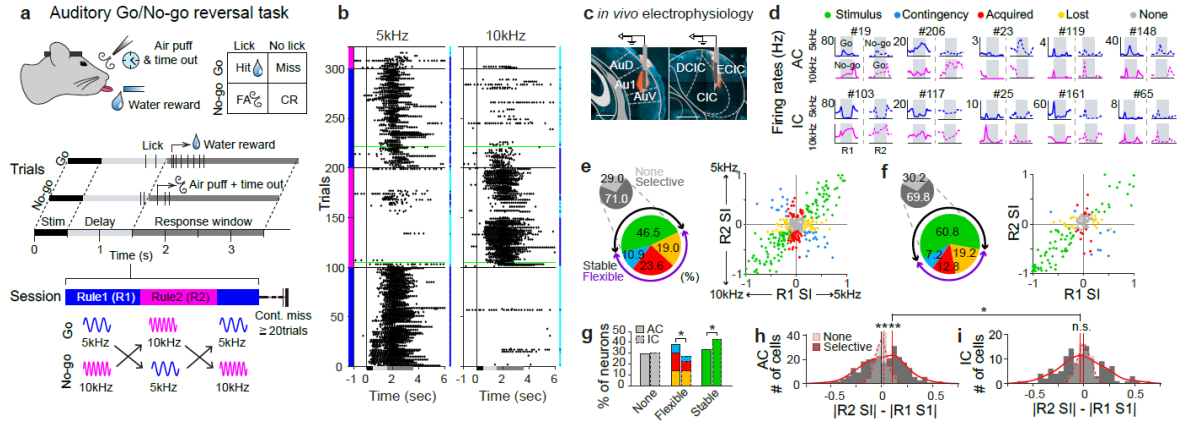

a. Schematic of the auditory Go/No-go reversal learning task.

b. Example lick raster plots from an expert mouse during a reversal learning session. Left, 5kHz trials; right, 10kHz trials. Each black dot represents a single lick event. Blue and magenta vertical bands denote R1 and R2 blocks, respectively. Vertical black lines at 0 s, sound onset; horizontal black lines, rule reversal point; green lines, TTRs; blue dots, lick trials; cyan dots, no-lick trials.

c. DiI-labeled brain sections showing multi-channel electrode tracks in the AC (left) and IC (right). AuD, secondary auditory cortex dorsal area; Au1, primary auditory cortex; AuV, secondary auditory cortex ventral area; DCIC, dorsal cortex of the inferior colliculus; CIC, central nucleus of inferior colliculus; ECIC, external cortex of the inferior colliculus. Scale bars, 500 µm.

d. Representative PSTHs of AC (top) and IC (bottom) neurons showing five types of SI changes across rules. From left to right, stimulus-selective (green), contingency-selective (blue), acquired selectivity (red), lost selectivity (yellow), and non-selective neurons. Blue, 5kHz trials; magenta, 10kHz trials; solid line, R1 trials; dotted line, R2 trials; gray shading, stimulus presentation epoch.

e. Left, fraction of neuronal types in AC (n=400 from 3 mice). Right, scatter plot showing SI values in R1 compared to R2 from individual neurons. Neuronal types were color-coded as in **d**.

f. Same as **e**, but for IC neurons (n=179 from 3 mice).

g. Proportions of non-selective, flexibly selective, and stably selective neurons in AC (solid bars) and IC (dotted bars). Neuronal types are color-coded as in **d**. Two-sided chi-squared test between AC and IC; flexible, p = 0.031; stable, p = 0.028.

h. Distribution of ΔSI across AC neurons. Light gray bars, non-selective neurons; dark gray bars, stimulus-selective neurons. Red lines, kernel density plots (dotted, non-selective neurons; solid, selective neurons). Vertical red line indicates the maximum density point for selective neurons (0.102). Non-selective neurons, $p = 0.2846$; selective neurons, $p = 8.81 \times 10^{-23}$; Sign test.

i. Same as **h**, but for the IC neurons (vertical red line at -0.040). Non-selective neurons, $p = 0.8919$; selective neurons, $p = 0.2392$; Sign test.

h-i. Statistical comparison of ΔSI values between AC and IC selective neurons. $p = 0.0488$; Mood's median test.

Fig. 2. Functional dissociation of AC and IC during auditory reversal learning

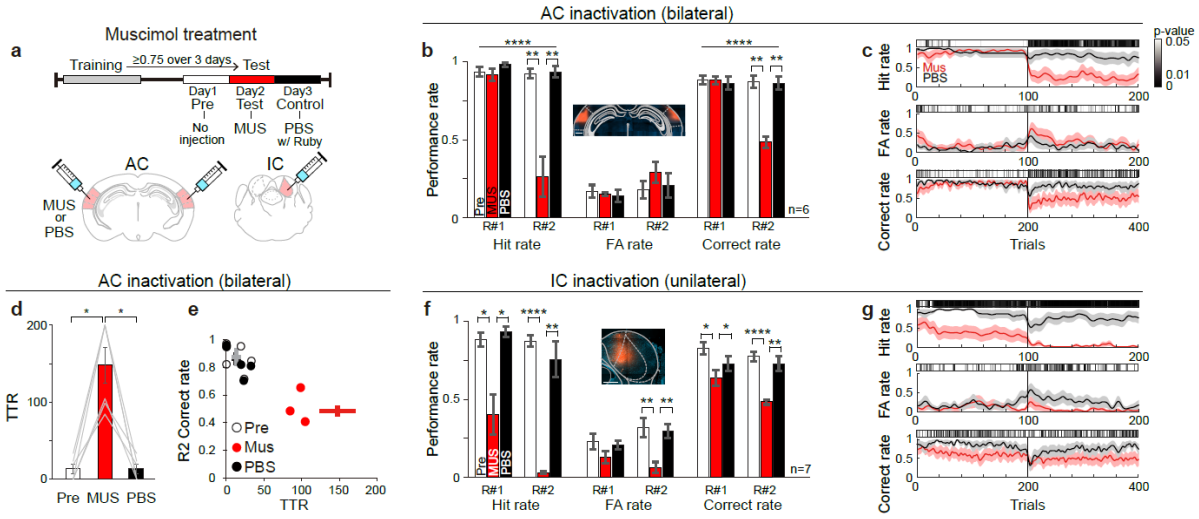

a. Schematic illustration of MUS or PBS injections into bilateral AC or unilateral IC for functional inactivation.

b. Behavioral performance changes during AC inactivation (N=6). Average Hit, FA, and Correct rates for Pre (no injection; open bars), MUS (red bars), and PBS (black bars) sessions. Repeated measures two-way ANOVA; Hit rate (drug, $p = 7.88 \times 10^{-7}$; rule, $p = 3.53 \times 10^{-5}$; interaction, $p = 6.69 \times 10^{-6}$); FA rate (drug, $p = 0.566$; rule, $p = 0.409$; interaction, $p = 0.850$); Correct rate (drug, $p = 1.04 \times 10^{-5}$; rule, $p = 9.3 \times 10^{-5}$; interaction, $p = 4.83 \times 10^{-6}$). Inset, bilateral AC areas co-injected with PBS and fluoro-ruby, aligned to Paxinos atlas (gray lines). Scale bar, 500 µm.

c. Average performance rates across a session. Top, Hit rate; middle, FA rate; bottom, correct rate. Red, MUS sessions; black, PBS sessions. Shaded areas indicate ± SEM. Top bars, gray-scaled p-values for significant differences between MUS and PBS sessions; Wilcoxon signed-rank test.

d. Average TTRs for Pre, MUS, and PBS sessions (mean ± SEM). Pre (13.42 ± 5.87) vs. MUS (148.08 ± 23.38), $p = 0.002$; MUS vs. Post (13.08 ± 5.70), $p = 0.004$; paired t-test.

e. Scatter plot of TTRs vs. R2 correct rates across sessions. Each circle represents a session; empty, Pre; red, MUS; black, PBS. Crosses, group means ± SEM.

f-g. same as **b-e**, but for IC inactivation (N=7). Repeated measures two-way ANOVA; Hit rate (drug, $p = 6.21 \times 10^{-11}$; rule, $p = 0.005$; interaction, $p = 0.067$); FA rate (drug, $p = 0.566$; rule, $p = 0.409$; interaction, $p = 0.850$); Correct rate (drug, $p = 2.99 \times 10^{-6}$; rule, $p = 0.044$; interaction, $p = 0.164$).

Fig. 3. PPC sends segregated top-down projections to both the AC and IC and is required for successful auditory reversal learning.

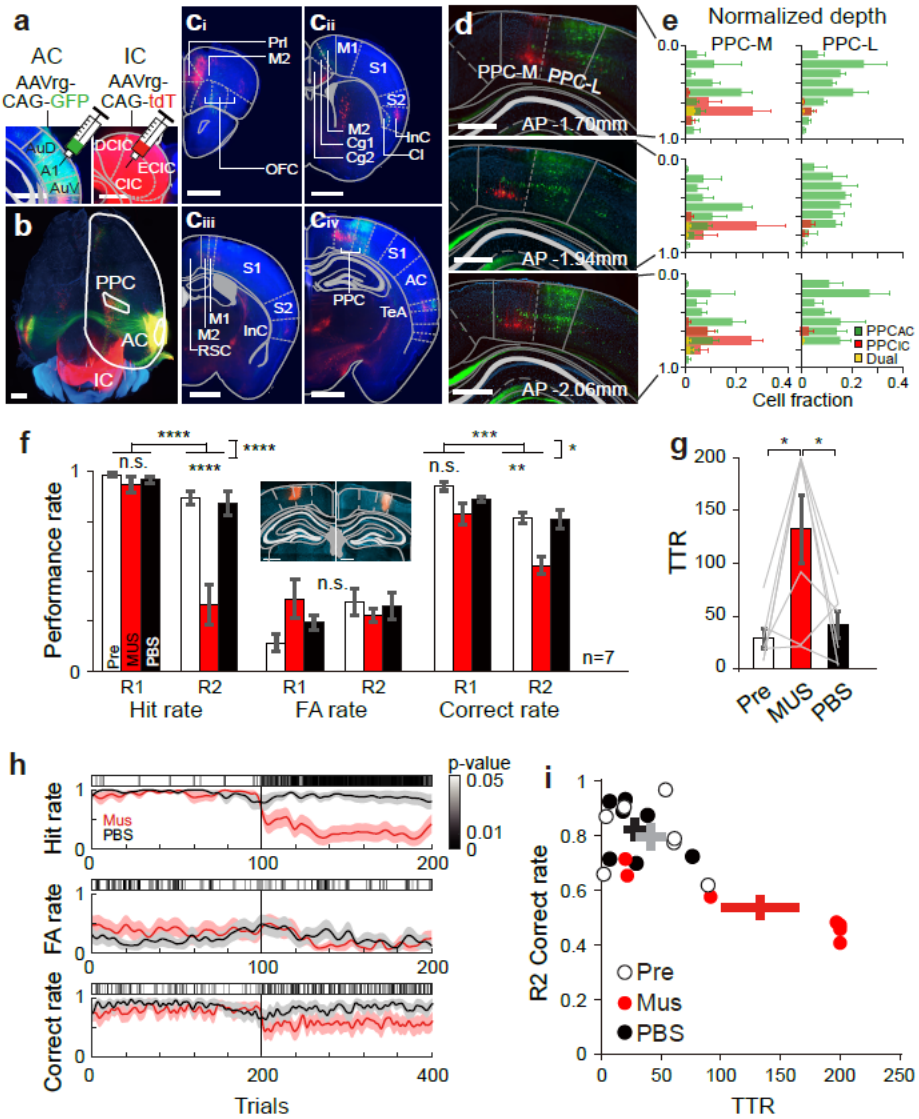

a-e. Dual-colored retrograde tracing reveals anatomically segregated PPC projections to the AC (green) and IC (red).

a. Coronal view of cleared whole brain showing injection sites in the AC (left, AAVrg-CAG-GFP) and IC (right, AAVrg-CAG-tdTomato), aligned to Paxinos atlas (gray lines). Scale bars, 500 µm.

b. Top view of the cleared brain. White lines demarcate the right cortical hemisphere and PPC. GFP-labeled PPC_{AC} neurons are located laterally; tdTomato-labeled PPC_{IC} neurons medially. Scale bar, 1 mm.

c. Coronal sections of the cleared brain imaged via light-sheet microscopy and reconstructed in 3D. DAPI (blue) constructs brain spaces; Retrogradely labeled AC-projecting neurons (green)

and IC-projecting neurons (red) are visualized across cortical areas. Images aligned to Paxinos atlas (gray lines). Scale bars, 1mm.

c_i, OFC (orbitofrontal cortex; medial, ventral, and lateral parts); Prl (prelimbic cortex); M2 (secondary motor cortex).

c_{ii}, M1 (primary motor cortex); M2; S1 (primary somatosensory cortex); S2 (secondary somatosensory cortex); Cg1 (cingulate cortex area 1); Cg2 (cingulate cortex area 2); InC (insular cortex); Cl (claustrum).

c_{iii}, M1; M2; S1; S2; InC.

c_{iv}, PPC (medial and lateral parts); S1; AC (dorsal and ventral parts); TeA (temporal association cortex).

d. Representative coronal sections of the PPC along the anterior-to-posterior (AP) axis showing distinct PPC_{AC} (green) and PPC_{IC} (red) populations. Images aligned to Paxinos atlas (gray lines). Scale bars, 500 µm.

e. Distribution of retrogradely labeled neurons in PPC-M (left) and PPC-L (right) across cortical layers and AP positions. Fractions of neurons were binned by cortical depth, normalized from pia (0) to ventricle (1) using DAPI signals. Green, PPC_{AC} neurons; red, PPC_{IC} neurons; yellow, dual-labeled neurons.

f-i. PPC inactivation impairs auditory reversal learning.

f. Behavioral performance changes during PPC inactivation (N=7), Average Hit, FA, and Correct rates for Pre (no injection; open bars), MUS (red bars), and PBS (black bars) sessions. Repeated measures two-way ANOVA; Hit rate: drug, $p = 3.84 \times 10^{-9}$; rule, $p = 1.83 \times 10^{-7}$; interaction, $p = 3.45 \times 10^{-8}$; FA rate: drug, $p = 0.666$; rule, $p = 0.423$; interaction, $p = 0.050$; Correct rate: drug, $p = 0.0001$; rule, $p = 0.001$; interaction, $p = 0.016$. Inset, fluoro-ruby co-injection site in bilateral PPC, aligned to Paxinos atlas (gray lines). Scale bars, 500 µm.

g. Average TTRs for Pre (no injection; 28.92 ± 9.08), MUS (133.21 ± 32.37), and PBS (42.29 ± 12.55) sessions (mean ± SEM). Paired t-test: Pre vs. MUS, $p = 0.019$; MUS vs. Post; $p = 0.034$.

h. Average performance rates across a session (N=7). Top, Hit rate; middle, FA rate; bottom, Correct rate. Red, MUS sessions; black, PBS sessions. Shaded areas indicate ± SEM. Top bars, gray-scale p-values for significant differences between MUS and PBS sessions; Wilcoxon signed-rank tests.

i. Scatter plot of TTRs vs. R2 correct rates across sessions. Circles, individual sessions (empty, Pre; red, MUS; black, PBS). Crosses, group means ± SEM.

854 **Fig. 4. Distinct population dynamics of PPC$_{AC}$ and PPC$_{IC}$ neurons during auditory**
855 **reversal learning**

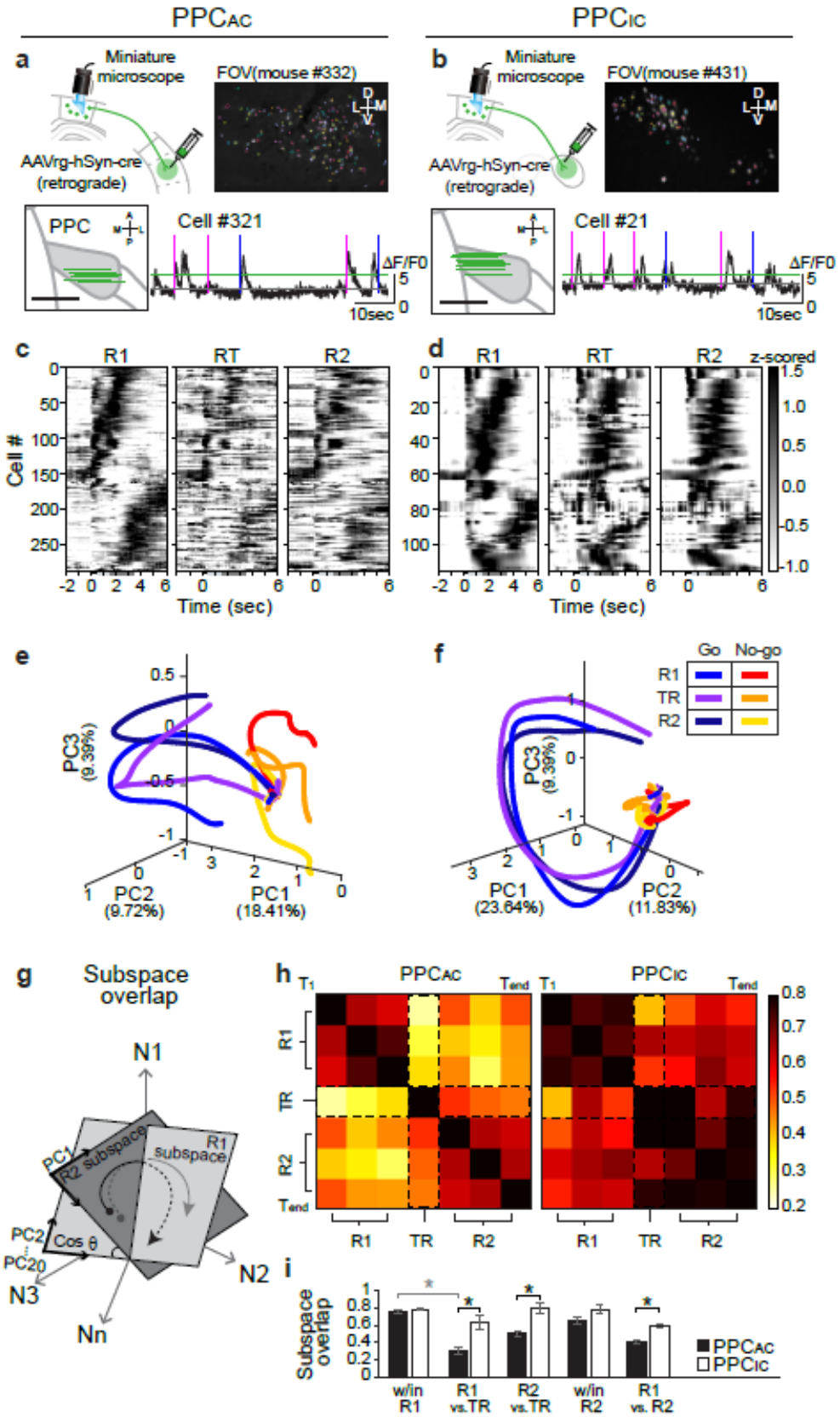

856

a. Top-left, schematic illustration of imaging PPC_{AC} neurons. Top-right, representative field of view (FOV) in PPC. Bottom left, top-view showing locations of all FOVs; scale bar, 1mm. Bottom right, example Ca^{2+} trace from a neuron during the task. Vertical blue and magenta lines indicate stimulus onset for 5kHz and 10kHz tones, respectively.

b. Same as **a**, but for imaging PPC_{IC} neurons.

c. Rastermap of trial-averaged and z-scored Ca^{2+} activity of PPC_{AC} neurons during Go trials in R1 (left), TR (middle), and R2 (right). Cells are clustered based on R1 activity.

d. Same as **c**, but for PPC_{IC} neurons.

e. PCA trajectories of trial-averaged PPC_{AC} population activity (aligned to stimulus onset, -2 to +6 s), projected onto the first three PCs. Colors represent trial types across task phases, as noted in the table.

f. Same as **e**, but for PPC_{IC} population activity.

g. Schematic illustration of the subspace overlap calculation method, based on angular differences between PC axes.

h. Subspace overlap heatmaps for PPC_{AC} (left) and PPC_{IC} (right) populations across task phases. Color scale indicates degree of overlap (0, no overlap; 1, complete overlap).

i. Average subspace overlaps (mean ± SEM) for PPC_{AC} (black bars) and PPC_{IC} (open bars) neurons within and across task phases. PPC_{AC} neurons showed significantly reduced overlap across rules (gray; $p = 0.0120$; Kruskal-Wallis ANOVA with multiple comparisons), and lower R1-R2 overlap compared to PPCIC neurons (0.374 ± 0.049 vs. 0.668 ± 0.045; $p < 0.001$, Wilcoxon rank-sum test), indicating more dynamic reorganization in the PPC_{AC} population. Note that PPC_{IC} neurons showed no significant difference between within- and across-rule overlaps.

Fig. 5. Distinct and multiplexed task variable encoding by PPC$_{AC}$ and PPC$_{IC}$ neurons during reversal learning.

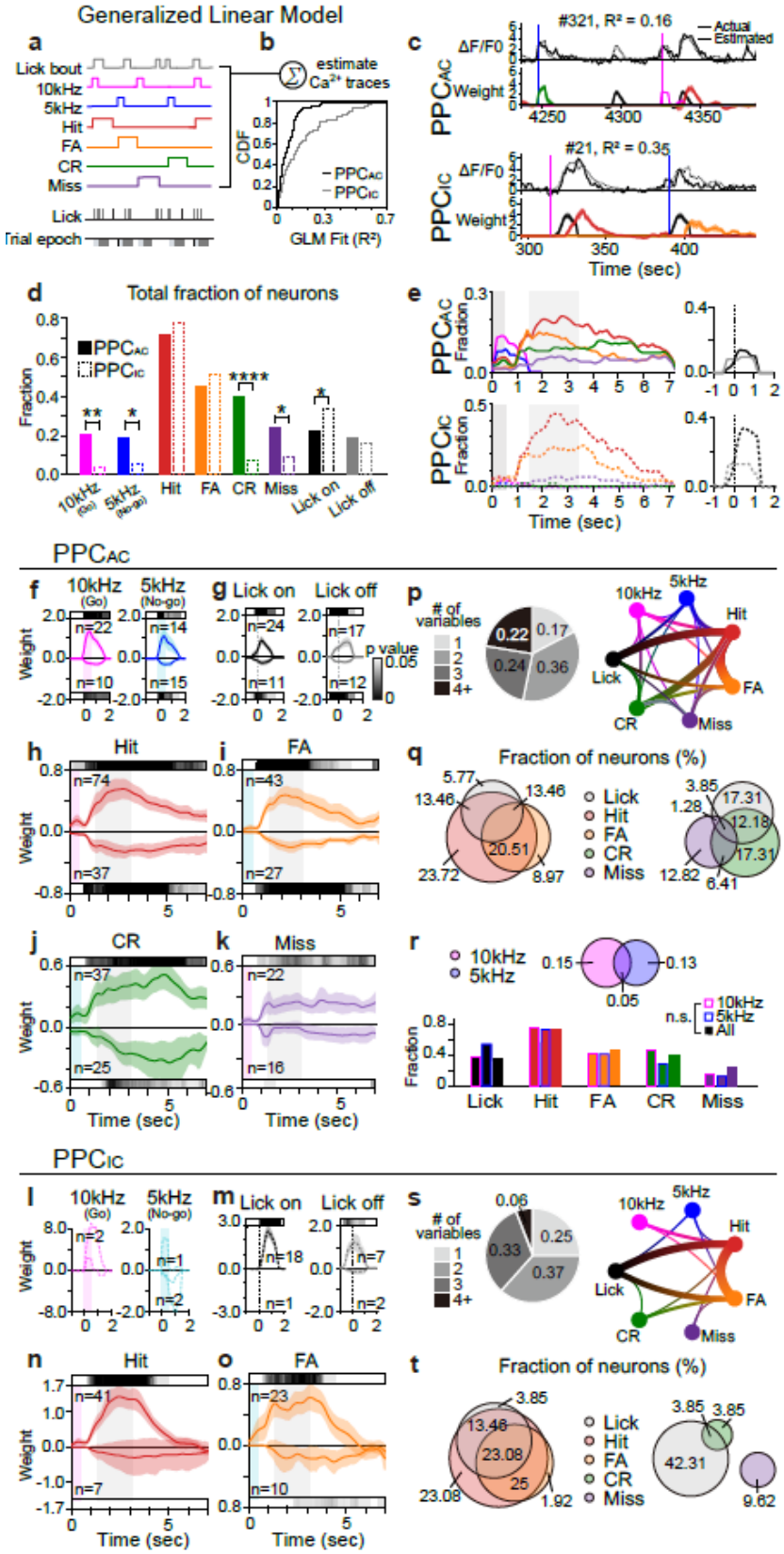

a. Schematic of the GLM analysis used to estimate how individual neurons encode task variables (TVs).

b. Cumulative distribution function of GLM-fitted R^2 values for PPC_{AC} (black) and PPC_{IC} (gray) neurons.

c. Example Ca^{2+} traces and corresponding GLM fits and TV weights from representative PPC_{AC} (**top**) and PPC_{IC} (**bottom**) neurons. Solid lines, measured Ca^{2+} signals; dotted lines, GLM-predicted activity. Vertical lines indicate stimulus onset (blue, 5kHz; magenta, 10kHz). Task variable weights are color-coded as in **a**.

d. Total fraction of neurons encoding each task variable. Filled bars, PPC_{AC}; open bars, PPC_{IC}. Two-sided chi-square test; 10kHz, $p = 0.004$; 5kHz, $p = 0.026$; CR, $p < 0.0001$; Miss, $p = 0.022$; Lick on, $p = 0.044$; Hit, FA and Lick off, not significant.

e. Time-resolved fractions of neurons encoding each task variable (color-coded) for PPC_{AC} (**top**) and PPC_{IC} (**bottom**) neurons. Left, stimulus and outcome encoding fractions across the trial epoch (0 to 7 s from stimulus onset). Gray shading, stimulus (dark) and response window (light) periods. Right, fractions of neurons encoding motor events (lick-on and lick-off at 0 s). Task variables are color-coded as in **a**.

f-k. Average GLM weights for PPC_{AC} neurons encoding specific task variables. Colored lines represent positive (**top**) or negative (**bottom**) weights; shades, SEM. Top and bottom bars, gray-scaled p-values for statistical significance compared to zero; one-sample Wilcoxon signed-rank test.

l-o. Same as **f-i**, but for PPC_{IC} neurons. When fewer than five neurons encoded a given variable, individual weight traces are shown as dotted lines.

p. Left, fraction of PPC_{AC} neurons grouped by the number of task variables encoded. Right, circular Sankey diagram showing TV co-encoding (multiplexing) patterns among PPC_{AC} neurons. Line thickness indicates frequency of each TV combination.

q. Proportional Euler diagrams showing overlap among PPC_{AC} neurons encoding Hit, FA, and lick variables (left) and CR, Miss, and lick variables (right).

r. Top, Euler diagrams of PPC_{AC} neurons encoding 10kHz and 5kHz stimuli. Bottom, comparison of co-encoding patterns among 10kHz-encoding (magenta outline), 5kHz-encoding (blue outline), and all TV-encoding (no outline) PPC_{AC} neurons. Bars show the fraction of co-encoding lick or outcome TVs. Two-sided chi-square test, not significant.

s-t. Same as **p-q**, but for PPC_{IC} neurons.

Fig. 6. Double dissociation of PPC top-down projections during auditory reversal learning

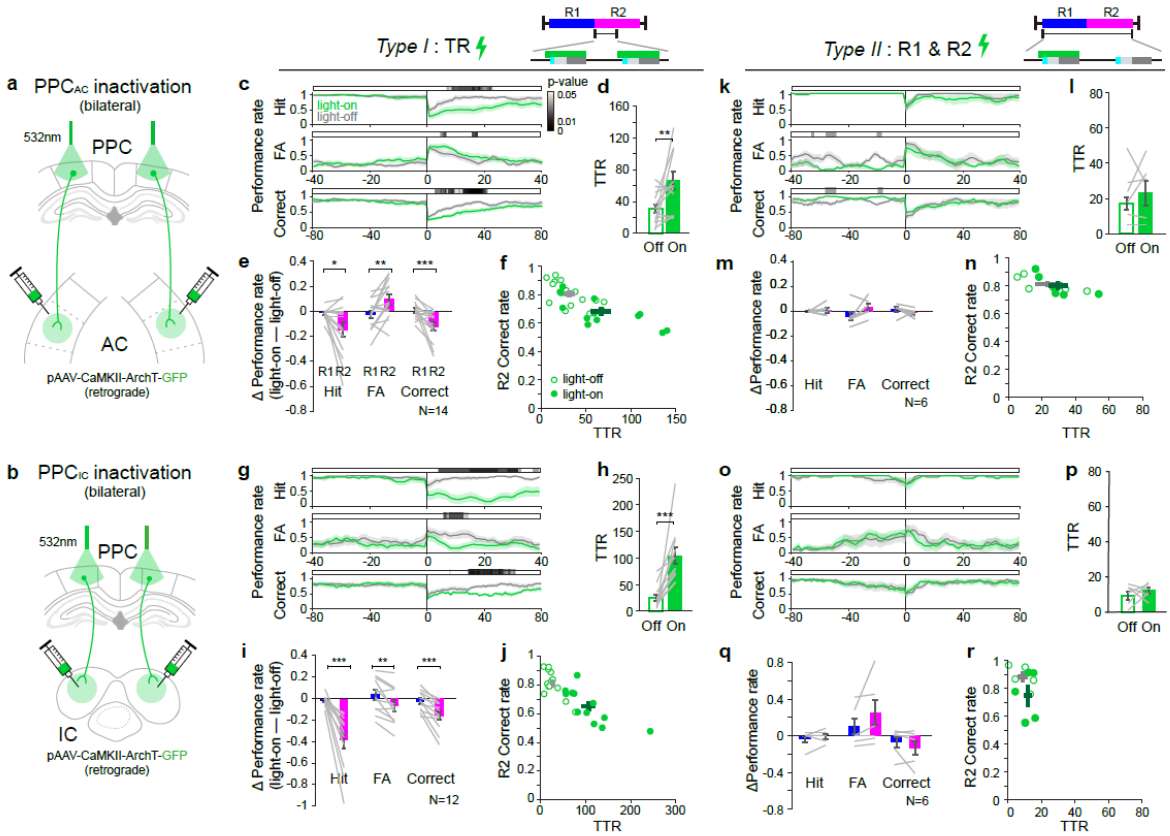

a-b. Schematic illustrations of optogenetic inactivation targeting PPC_{AC} neurons (**a**) and PPC_{IC} neurons (**b**)

c-f. Impaired reversal learning induced by Type I PPC_{AC} inactivation (N=14). Top, Type I inactivation protocol. Green laser light was delivered in a block of 40 to 80 trials immediately following the rule reversal, from 1 s before stimulus onset to the end of the response window.

c. Time course of Hit rate (top), FA rate (middle), and correct rate (bottom) across task phases, aligned to the R2 start (trial 0). Green lines, light-on sessions; gray lines, light-off sessions; shades, ± SEM. Top bars, gray-scaled p-values for significant differences between light-off and light-on sessions; Wilcoxon signed-rank test.

d. TTRs increased in light-on sessions (66.79 ± 10.98) compared to light-off sessions (31.29 ± 5.37); p = 0.009, Wilcoxon signed-rank test.

e. Δ Performance rate (light-on minus light-off) for Hit (R1, -0.015 ± 0.011; R2, -0.148 ± 0.057; p = 0.042), FA (R1 = -0.027 ± 0.032; R2 = 0.096 ± 0.040; p = 0.007), and Correct rates (R1, 0.005 ± 0.019; R2, -0.167 ± 0.052; p = 0.001). Wilcoxon signed-rank test.

f. Scatter plot of TTR vs. R2 correct rate per session. Green-filled circles, light-on; green-empty

circles, light-off. Crosses represent group mean ± SEM (dark-green, light-on; gray, light-off).

g-j. Same as **c-f**, but for Type I PPC_{IC} inactivation (N=12).

h. TTRs increased in light-on sessions (104.08 ± 14.95) compared to light-off sessions (25.08 ± 5.94); p = 0.0005, Wilcoxon signed-rank test.

i. Δ Performance rate for Hit (R1, -0.022 ± 0.015; R2, -0.388 ± 0.077; p = 0.0005), FA (R1 = 0.032 ± 0.045; R2 = -0.069 ± 0.049; p = 0.003), and Correct rates (R1, -0.027 ± 0.027; R2, -0.160 ± 0.038; p = 0.0005). Wilcoxon signed-rank test.

k-n. Same as **c-f** but for Type II PPC_{AC} inactivation (N=6). Top, Type II inactivation protocol. Green laser light was delivered randomly in 50% of trials across rules, from 1 s before stimulus onset to the end of the response window. Note that mice showed intact reversal learning.

l. TTRs were not significantly different between light-on (29.33 ± 5.58) and light-off (23.00 ± 6.84) sessions.

m. Δ Performance rates for Hit (R1, 0.003 ± 0.003; R2, 0.010 ± 0.018; n.s.), FA (R1 = -0.036 ± 0.037; R2 = 0.0.35 ± 0.030; n.s.), and Correct rates (R1, 0.019 ± 0.019; R2, -0.012 ± 0.014; n.s.).

o-p. Same as **d-g** but for Type II PPC_{IC} inactivation (N=6). Note that mice showed intact reversal learning.

p. TTRs were not significantly different between light-on (9.40 ± 2.29) and light-off (12.40 ± 1.74) sessions.

q. Δ Performance for Hit (R1, -0.035 ± 0.035; R2, -0.010 ± 0.026; n.s.), FA (R1 = 0.105 ± 0.085; R2 = 0.253 ± 0.138; n.s.), and Correct rates (R1, -0.072 ± 0.057; R2, -0.131 ± 0.074; n.s.).

956 **Extended data figures**

957 **Extended Data Figure 1. Behavioral adaptation and performance dynamics in mice**
958 **during within-session auditory reversal learning**

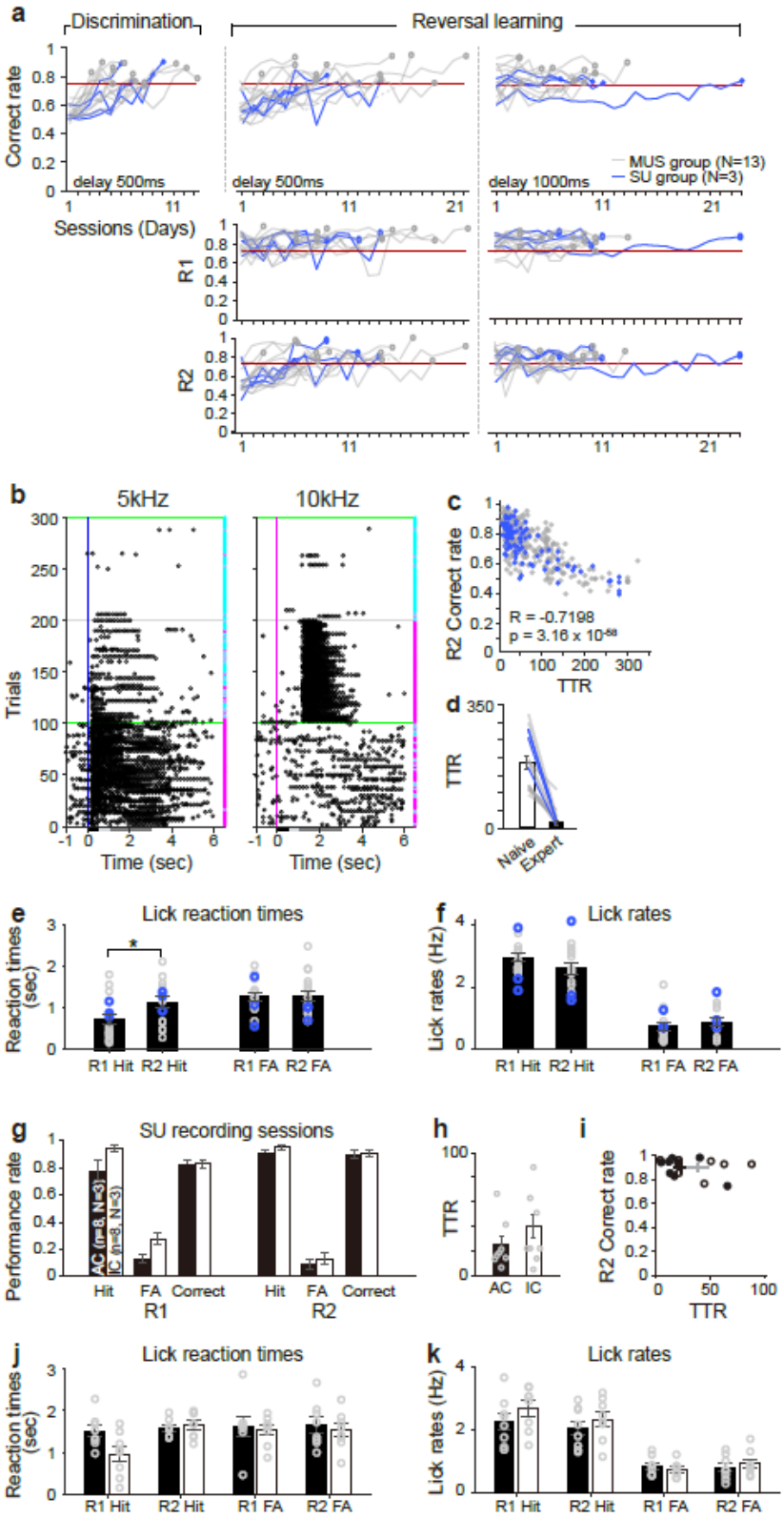

959

a. Performance changes in mice during auditory reversal learning. Top, correct rates across training stages in 16 mice used for single-unit recordings (N=3, blue) and MUS experiments (N=13, gray). Left, auditory discrimination (R1 only) with a 500 ms response window delay; middle, reversal learning with a 500 ms delay; right, reversal learning with a 1000 ms delay. Red horizontal lines indicate expert-level performance threshold (correct rate ≥ 0.75). Bottom, correct rates for R1 and R2 trials during reversal learning with a 500 ms (left) and 1000 ms (right) delays.

b. Representative lick raster plots from an example mouse (same as in Fig. 1b) on the first day of training the reversal learning task. Each dot represents a single lick event. Green lines indicate rule switch trials and gray line indicates where conditioning trial end. Note that mice started to lick when the water reward was passively given (before gray line) after the delay period in R2.

c. Scatter plot of TTR vs. R2 correct rate across all training sessions. Each circle indicates a session; red dashed line shows linear regression across all data points. A negative Pearson's correlation indicates performance improvement over training.

d. Average TTRs for naïve (189.82 ± 19.04) versus expert (30.82 ± 6.25) mice, showing significantly faster adaptation in trained animals.

e. Lick reaction times for Hit and FA trials. A significant delay in R2 Hit trials compared to R1 ($p = 0.0275$), but not in FA trials. Wilcoxon rank-sum test.

f. Lick rates for Hit and FA trials, showing no significant differences across rules.

g. Average Hit rate, FA rate, and overall correct rate in mice recorded from AC (N=3, n=8 sessions; black bars) and IC (N=3, n=9 sessions; open bars). No significant differences were observed between groups (two-way ANOVA without repetition).

h. Average TTRs for AC-recorded (24.37 ± 6.95) and IC-recorded (42.66 ± 10.16) sessions. Circles, individual recording sessions.

i. Scatter plot of TTRs vs. R2 correct rates across all sessions (AC = 0.87 ± 0.04; IC = 0.93 ± 0.01). Circles, individual sessions (black, AC; empty, IC); crosses, group means ± SEM.

j-k. Lick reaction times (j) and lick rates (k) for Hit and FA trials across sessions. Circles, individual sessions; black bars, AC-recorded sessions; open bars, IC-recorded sessions. No significant group differences (Wilcoxon rank-sum test).

Extended Data Figure 2. Validation of MUS inactivation effects on behavioral performance

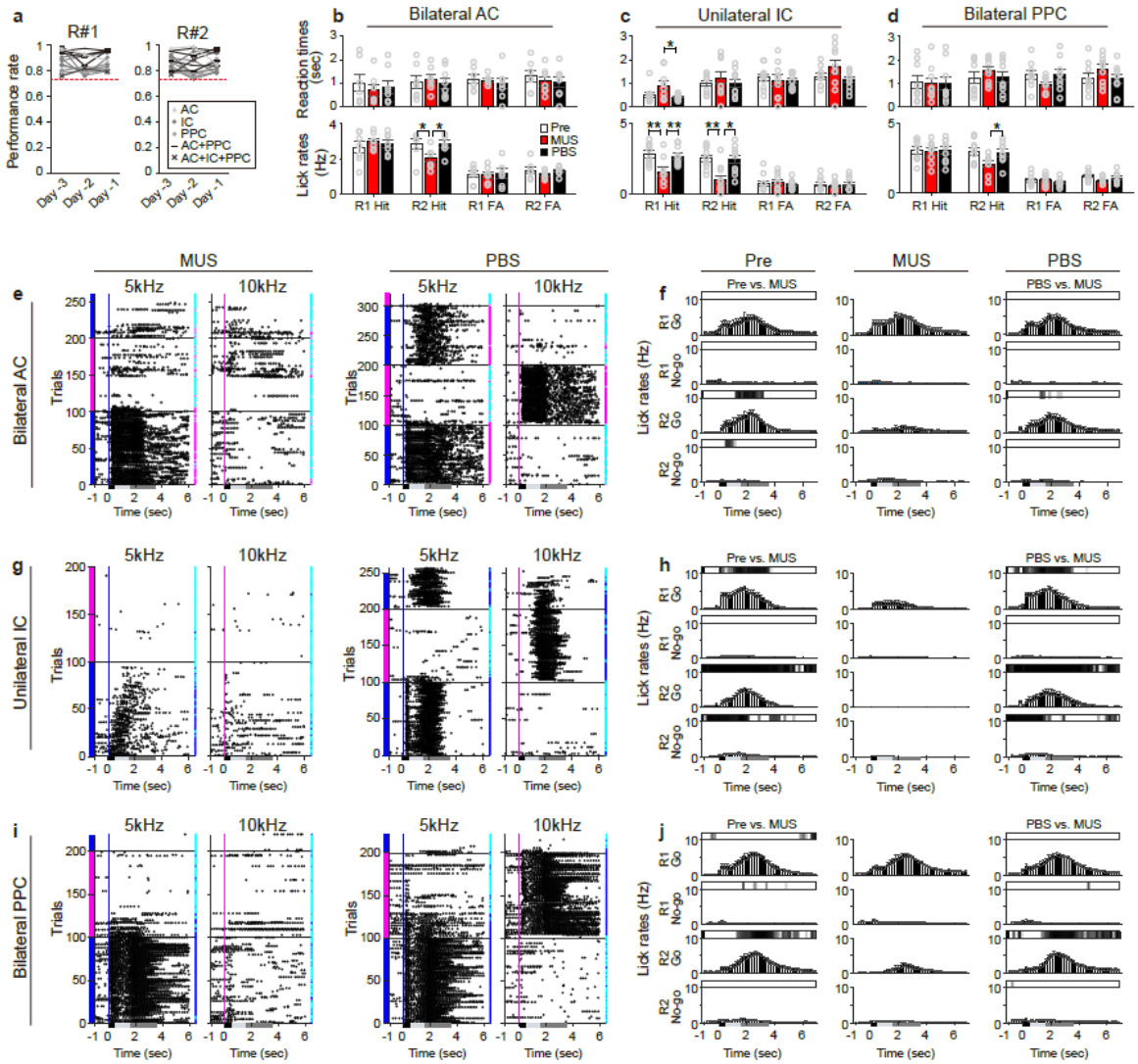

a. Baseline performance prior to MUS inactivation. Mice achieved correct rates > 0.75 for both rules across three consecutive days before MUS injections into AC, IC, or PPC.

b. Lick reaction times (Top) and lick rates (Bottom) for Hit and FA trials during AC inactivation. Circles, individual sessions; open bars, Pre sessions; red bars, MUS sessions, black bars, PBS sessions. Wilcoxon rank-sum test; lick rates for R2 Hit trials, Pre vs. MUS ($p = 0.034$); Mus vs. PBS ($p = 0.024$).

c. Same as **b**, but for IC inactivation sessions. Wilcoxon rank-sum test; reaction times of R1 Hit trials, MUS vs. PBS ($p = 0.053$); lick rates of R1 Hit trials, Pre vs. MUS ($p = 0.008$); MUS vs. PBS ($p = 0.010$); lick rates of R2 Hit trials, Pre vs. MUS ($p = 0.004$); MUS vs. PBS ($p = 0.013$).

d. Same as **b**, but for PPC inactivation sessions. Wilcoxon rank-sum test; lick rates of R2 Hit trials, MUS vs. PBS ($p = 0.019$).

e. Example lick raster plots from AC inactivation sessions. Left, MUS injection; right, PBS injection.

f. Session-averaged lick histograms for Hit and FA trials during Pre (left), MUS (middle), and PBS (right) injection sessions targeting bilateral AC. Top bars, gray-scaled p-values representing statistical significance relative to MUS sessions (Wilcoxon signed-rank test).

g-h. Same as **e-f**, but for IC inactivation sessions.

i-j. Same as **e-f**, but for PPC inactivation sessions.

1014 **Extended Data Figure 3. Quantification of projection-specific PPC neurons**

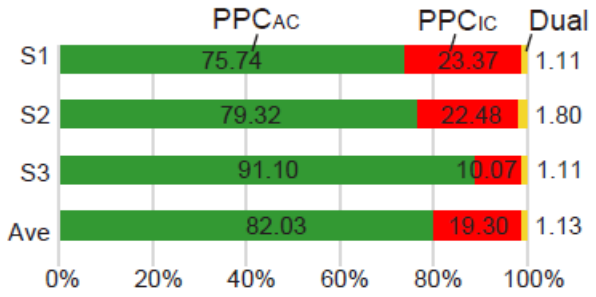

1015

1016 Proportions (%) of PPC_{AC}, PPC_{IC}, and dual-projecting neurons across individual brain samples
1017 (S1-S3, N=3) and group average (bottom).

1018

1019 **Extended Data Figure 4. Behavioral performance during in vivo imaging of PPC_{AC} and**
1020 **PPC_{IC} neurons and robustness of neural population analyses**

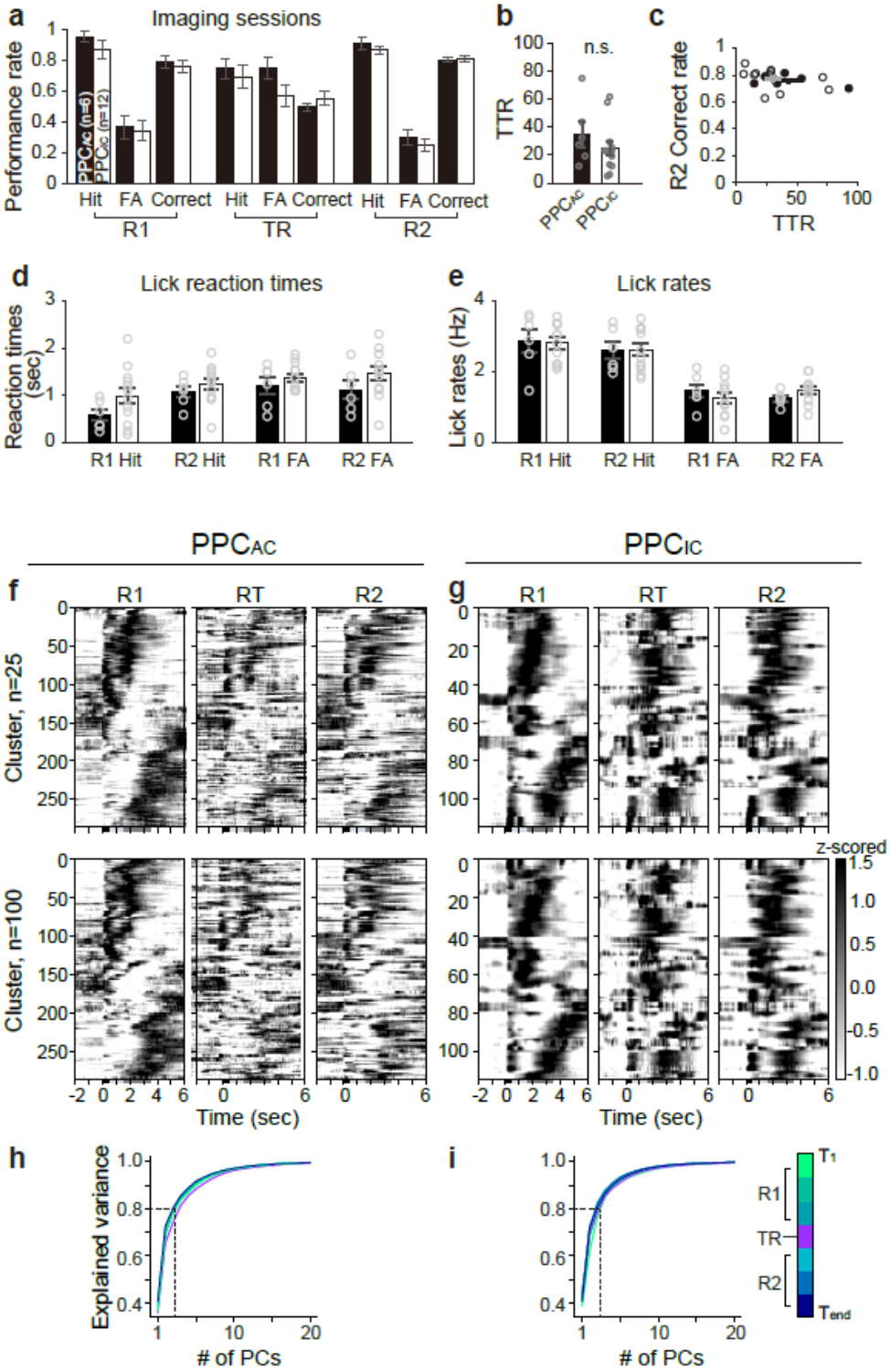

1021

1022 **a.** Average Hit rate, FA rate, and Correct rate for mice in the PPC_{AC} (n=6, black bars) and PPC_{IC}
1023 (n=12, open bars) imaging groups. No significant differences observed between groups (two-
1024 way ANOVA without repetition).

b. Average TTRs for PPC_{AC} (34.50 ± 9.02) and PPC_{IC} (24.58 ± 5.12) imaging sessions. Circles, individual sessions.

c. Scatter plot of TTRs vs. R2 correct rates across all imaging sessions ($PPC_{AC,}$ 0.76 ± 0.01; PPC_{IC}, 0.77 ± 0.02). Circles, individual sessions (black, PPC_{AC}; empty, PPC_{IC}); crosses, group means ± SEM (black, PPC_{AC}; gray, PPC_{IC}).

d-e. Lick reaction times **(d)** and lick rates **(e)** for Hit and FA trials across imaging sessions. Circles, individual sessions; black bars, PPC_{AC} sessions; open bars, PPC_{IC} sessions. No significant group differences (Wilcoxon rank-sum test).

f-g. Rastermap clustering of PPC_{AC} (a) and PPC_{IC} (b) neurons with the number of clusters set to 25 (top) and 100 (bottom). Dynamic shifts in PPC_{AC} activity and stable patterns in PPC_{IC} were consistently observed across clustering resolutions, confirming the robustness of population dynamics shown in **Fig. 3c-d**.

h-i. Explained variance from PCA of Ca^{2+} activity in PPC_{AC} (c) and PPC_{IC} (d) neurons across task phases (same dataset as in **Fig. 3h**). The first 20 PCs accounted for ~80% of total variance, supporting the choice of 20 PCs for subspace overlap calculations in **Fig. 3h**.

Extended Data Figure 5. Temporal dynamics of task variable encoding in projection-specific PPC populations across rules

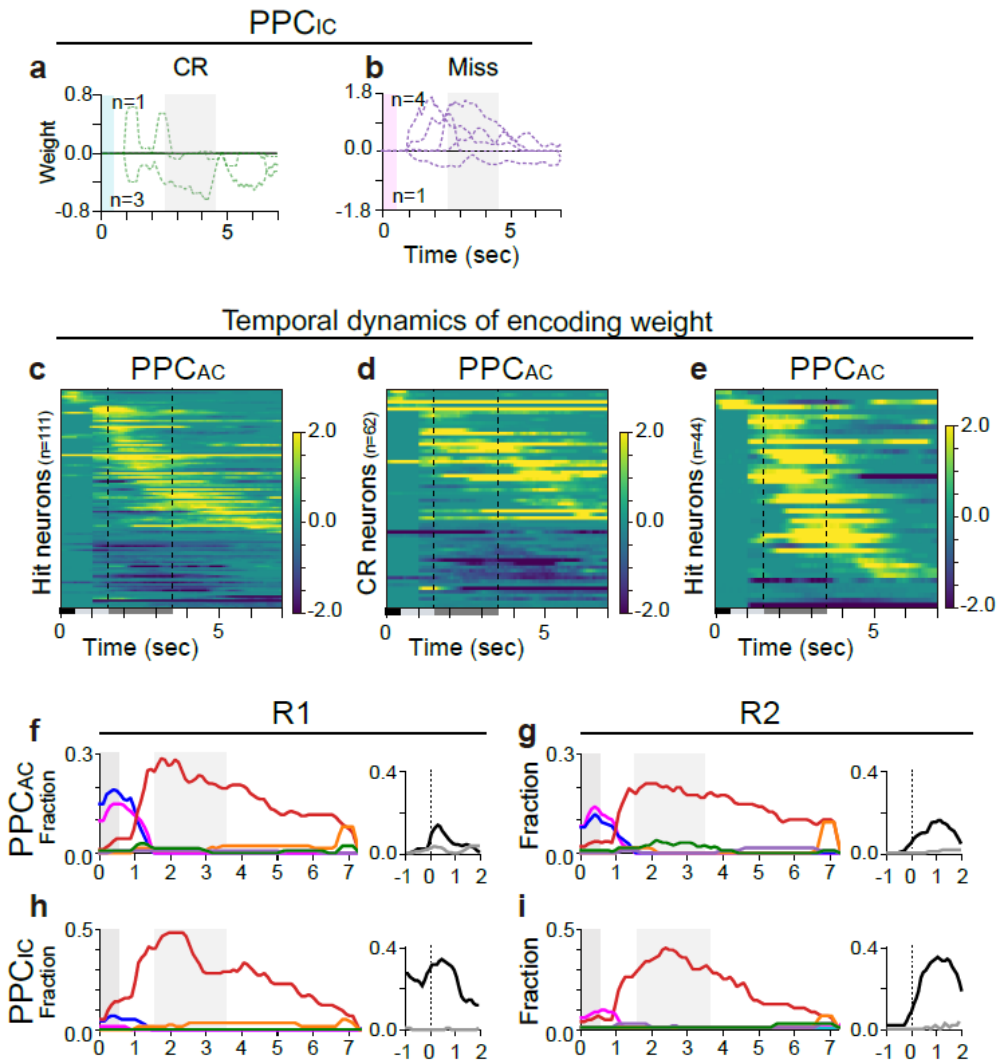

a-b. Averaged positive and negative GLM weights for CR- (**a**) and Miss-encoding (**b**) PPC_{IC} neurons. For task variables with fewer than 5 encoding neurons, individual weights are shown.

c-e. Time-varying GLM weights sorted by peak amplitude for Hit-encoding (**c**), CR-encoding (**d**) PPC_{AC} neurons, and Hit-encoding PPC_{IC} neurons (**e**). Black vertical lines at 0 s indicate sound onset; dotted vertical lines at 1.5 s and 3.5 s denote the start and end of the response window.

f-g. Time-resolved fractions of neurons encoding each task variable (color-coded) in PPC_{AC} neurons during R1 (**f**) and R2 (g), aligned to stimulus onset. Right, fractions of neurons encoding lick-bout onset (black) and offset (gray), aligned to their respective motor events.

h-i. Same as **f-g,** but in PPC_{IC} neurons.

Extended Data Figure 6. Control experiment for optogenetic manipulations of PPC_{AC} and PPC_{IC} circuits during auditory reversal learning performance

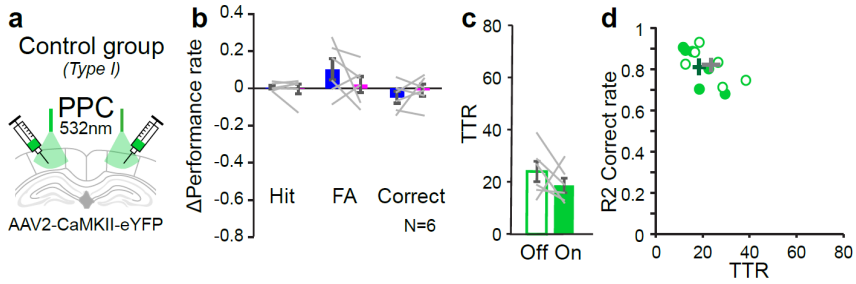

a-c. Control green-light (532 nm) stimulation of the PPC during Type I optogenetic inhibition experiments.

a. Δ Performance rates between light-on and light-off sessions for Hit (R1, 0.006 ± 0.009; R2, -0.002 ± 0.026; n.s.), FA (R1 = 0.102 ± 0.057; R2 = 0.021 ± 0.043; n.s.), and Correct rates (R1, -0.049 ± 0.032; R2, -0.010 ± 0.032; n.s.). Wilcoxon signed-rank test.

b. TTRs in light-off sessions (24.00 ± 3.89) and light-on sessions (18.83 ± 2.77); p = 0.009. Wilcoxon signed-rank test.

c. Scatter plot of TTRs vs. R2 correct rates. Green-empty circles, light-off sessions; green-filled circles, light-on sessions; Crosses, mean ± SEM (gray, light-off; dark green, light-on)

1067 **Supplementary Movies**

1068 **Supplementary movie 1. 3D view of a whole mouse brain injected with retrograde tracers**
1069 **in AC and IC**

1070 360-degree rotation of a cleared whole mouse brain around the mediolateral (ML) axis, with a
1071 fixed anteroposterior (AP) position.

1072

1073 **Supplementary movie 2. Mapping neurons projecting to AC and IC in whole mouse**
1074 **brains**

1075 Series of coronal sections from five cleared whole mouse brain samples, progressing from
1076 posterior to anterior regions. The central sample corresponds to the one shown in **Fig. 3** and
1077 **Supplementary movie 1**, aligned to the Paxinos brain atlas. Scale bars: 1 mm. Note that
1078 images appear left-right reversed due to microscope orientation. Green fluorescence indicates
1079 AC-projecting neurons, while red fluorescence marks IC-projecting neurons. Key anatomical
1080 structures include: central nucleus of inferior colliculus (CIC); external cortex of inferior
1081 colliculus (ECIC); dorsal cortex of inferior colliculus (DCIC); auditory cortex including
1082 primary (A1), dorsal (AuD), and ventral (AuV) regions; primary (S1) and secondary (S2)
1083 somatosensory cortices; primary (M1) and secondary (M2) motor cortices; cingulate cortex
1084 areas 1 and 2 (Cg1, Cg2); insular cortex (InC); claustrum (Cl); infralimbic cortex (IL);
1085 prelimbic cortex (PrL); and orbitofrontal cortex (OFC) with medial (m), ventral (v), and lateral
1086 (l) subdivisions.

1087 **Supplementary Data Tables**

1088 **Supplementary Data Table 1. Behavior performance rates and TTRs of mice used for**
1089 **electrophysiology**

			R#1			R#2			
Target	mouse #	# of neurons	Hit rate	FA rate	Correct rate	Hit rate	FA rate	Correct rate	TTR
AC	602	40	1.00	0.11	0.95	0.95	0.06	0.95	21
		42	0.66	0.16	0.75	1.00	0.03	0.99	41
		56	0.68	0.01	0.84	0.91	0.02	0.95	6
	605	37	0.96	0.16	0.90	0.97	0.01	0.98	16
		89	0.93	0.17	0.88	0.80	0.31	0.75	66
		64	0.42	0.01	0.71	0.77	0.11	0.83	18
	606	37	0.91	0.18	0.86	0.86	0.15	0.86	14
		35	0.69	0.25	0.72	0.97	0.07	0.95	13
AC total	N=3	400	0.78 ± 0.03	0.17 ± 0.04	0.83 ± 0.03	0.90 ± 0.03	0.10 ± 0.04	0.90 ± 0.03	24.38 ± 6.95
IC	602	22	0.93	0.26	0.84	0.95	0.42	0.77	45
		58	0.83	0.41	0.71	1.00	0.14	0.93	63
		13	0.97	0.41	0.78	0.98	0.12	0.93	22
	606	9	0.96	0.07	0.95	0.96	0.05	0.96	51
		20	1.00	0.22	0.89	0.85	0.14	0.86	22
		23	1.00	0.19	0.91	0.96	0.03	0.97	5
		24	1.00	0.24	0.88	0.97	0.04	0.97	22
	609	10	0.86	0.44	0.71	0.96	0.10	0.93	88
IC total	N=3	179	0.94 ± 0.02	0.28 ± 0.05	0.83 ± 0.03	0.95 ± 0.02	0.13 ± 0.04	0.91 ± 0.02	39.75 ± 9.61

1090

1091

1092 **Supplementary Data Table 2. Behavior performance rates and TTRs of mice used for**
1093 **MUS experiments**

			R1						R2							
Target	# of mouse	Session	Hit rate		FA rate		Correct rate		Hit rate		FA rate		Correct rate		TTR	
			Mean	±	Mean	±	Mean	±	Mean	±	Mean	±	Mean	±	Mean	±
AC	6	Pre	0.94	0.03	0.17	0.04	0.88	0.03	0.93	0.03	0.18	0.06	0.87	0.04	13.42	5.87
		MUS	0.92	0.04	0.15	0.01	0.88	0.03	0.26	0.13	0.29	0.07	0.49	0.04	148.08	23.38
		PBS	0.98	0.01	0.14	0.04	0.92	0.02	0.94	0.04	0.21	0.08	0.86	0.04	13.08	5.70
IC	7	Pre	0.88	0.05	0.23	0.05	0.83	0.04	0.87	0.04	0.32	0.06	0.77	0.03	16.71	6.03
		MUS	0.40	0.13	0.13	0.04	0.64	0.05	0.03	0.01	0.06	0.04	0.48	0.02	187.29	12.71
		PBS	0.93	0.03	0.21	0.03	0.86	0.02	0.76	0.12	0.30	0.05	0.73	0.05	29.50	10.42
PPC	7	Pre	0.99	0.01	0.13	0.03	0.93	0.01	0.96	0.01	0.32	0.08	0.82	0.04	28.93	9.08
		MUS	0.94	0.03	0.35	0.10	0.80	0.06	0.31	0.34	0.20	0.03	0.55	0.04	133.21	32.37
		PBS	0.96	0.02	0.24	0.03	0.86	0.01	0.90	0.05	0.32	0.09	0.79	0.05	42.29	12.55

1094

1095

Supplementary Data Table 3. Behavior performance rates and TTRs of mice used for Ca^{2+} imaging

		R1			TR			R2			
Group	# of neurons (CMFE, Manual ROI)	Hit rate	FA rate	Correct rate	Hit rate	FA rate	Correct rate	Hit rate	FA rate	Correct rate	TTR
PPC_{AC}	149	0.99	0.50	0.75	0.77	0.92	0.42	0.97	0.39	0.79	27
	180	0.98	0.18	0.90	0.60	0.50	0.55	0.98	0.48	0.75	12
	92	1.00	0.27	0.87	0.85	0.82	0.50	0.84	0.18	0.83	43
	54	0.80	0.38	0.71	0.57	0.58	0.49	0.74	0.18	0.78	74
	72	0.97	0.66	0.66	1.00	0.81	0.58	0.98	0.29	0.85	32
	47	0.98	0.22	0.88	0.70	0.88	0.44	0.92	0.28	0.82	19
PPC_{AC} total	594	0.95 ± 0.03	0.37 ± 0.08	0.79 ± 0.04	0.75 ± 0.07	0.75 ± 0.07	0.50 ± 0.02	0.90 ± 0.04	0.30 ± 0.05	0.80 ± 0.01	34.5 ± 9.02
PPC_{IC}	57	1.00	0.38	0.81	0.80	0.75	0.50	0.87	0.14	0.86	23
	37	1.00	0.78	0.61	0.73	0.82	0.45	1.00	0.22	0.89	23
	5	1.00	0.39	0.81	1.00	0.67	0.60	0.98	0.19	0.90	6
	4	0.99	0.09	0.95	0.83	0.67	0.58	0.95	0.29	0.83	13
	1	1.00	0.18	0.91	0.83	0.75	0.54	0.92	0.32	0.80	25
	13	0.61	0.65	0.48	0.50	0.64	0.43	0.89	0.51	0.69	29
	14	0.76	0.24	0.76	1.00	0.00	1.00	0.82	0.20	0.81	5
	10	0.94	0.41	0.77	0.89	0.71	0.59	0.78	0.07	0.85	57
	27	0.99	0.34	0.83	0.50	0.70	0.39	0.79	0.50	0.65	19
	11	0.35	0.17	0.59	0.36	0.30	0.52	0.76	0.10	0.83	22
	10	0.88	0.08	0.90	0.67	0.60	0.55	0.82	0.18	0.82	12
	5	0.93	0.43	0.75	0.17	0.23	0.47	0.75	0.22	0.76	61
PPC_{IC} total	194	0.87 ± 0.06	0.34 ± 0.06	0.76 ± 0.04	0.69 ± 0.07	0.57 ± 0.07	0.55 ± 0.05	0.86 ± 0.02	0.25 ± 0.04	0.81 ± 0.02	24.58 ± 5.12

Supplementary Data Table 4. Behavior performance rates and TTRs of mice used for optogenetic manipulations

				R1						R2							
Group	# of mouse	Type	Condition	Hit rate		FA rate		Correct rate		Hit rate		FA rate		Correct rate		TTR	
				Mean	±	Mean	±	Mean	±	Mean	±	Mean	±	Mean	±	Mean	±
PPC_{AC}	14	Type I	Light on	0.96	0.02	0.22	0.05	0.87	0.02	0.74	0.06	0.37	0.04	0.68	0.03	66.79	10.98
			Light off	0.98	0.01	0.25	0.05	0.86	0.02	0.88	0.03	0.28	0.05	0.80	0.02	31.29	5.37
	6	Type I - ITI	Light on	0.97	0.02	0.23	0.05	0.87	0.03	0.77	0.07	0.40	0.09	0.69	0.05	50.67	4.48
			Light off	0.99	0.01	0.29	0.06	0.85	0.03	0.91	0.05	0.34	0.10	0.78	0.04	32.67	5.21
	6	Type II	Light on	1.00	0.04	0.12	0.04	0.94	0.02	0.92	0.04	0.34	0.08	0.79	0.03	23.00	6.84
			Light off	1.00	0.00	0.15	0.05	0.92	0.02	0.90	0.05	0.31	0.06	0.80	0.02		
	5	Type II - ITI	Light on	0.96	0.06	0.13	0.06	0.92	0.03	0.93	0.06	0.30	0.08	0.82	0.05	20.00	3.05
			Light off	0.98	0.01	0.14	0.07	0.92	0.04	0.91	0.06	0.31	0.08	0.80	0.05		
PPC_{IC}	14	Type I	Light on	0.95	0.02	0.24	0.05	0.85	0.03	0.51	0.08	0.21	0.04	0.65	0.04	104.08	14.95
			Light off	0.97	0.01	0.22	0.04	0.88	0.02	0.91	0.03	0.29	0.03	0.81	0.02	24.57	5.09
	9	Type I - ITI	Light on	0.97	0.02	0.30	0.05	0.84	0.03	0.58	0.10	0.25	0.05	0.66	0.04	90.11	25.78
			Light off	0.98	0.01	0.24	0.06	0.87	0.03	0.95	0.02	0.28	0.04	0.84	0.03	19.89	4.09
	5	Type II	Light on	0.95	0.04	0.40	0.11	0.77	0.07	0.94	0.02	0.46	0.15	0.74	0.08	12.40	2.14
			Light off	0.98	0.01	0.30	0.07	0.84	0.04	0.95	0.03	0.21	0.08	0.87	0.04		
	5	Type II - ITI	Light on	1.00	0.00	0.14	0.06	0.93	0.03	0.94	0.03	0.32	0.09	0.81	0.05	24.20	8.10
			Light off	0.99	0.01	0.15	0.08	0.92	0.04	0.96	0.02	0.27	0.04	0.85	0.02		
PPC_{ctrl}	6	Type I	Light on	0.98	0.01	0.29	0.07	0.85	0.04	0.93	0.03	0.29	0.05	0.82	0.04	18.83	2.77
			Light off	0.98	0.02	0.19	0.06	0.89	0.03	0.93	0.03	0.27	0.05	0.83	0.03	24.00	3.89
	6	Type I - ITI	Light on	0.99	0.01	0.28	0.07	0.85	0.04	0.98	0.00	0.29	0.07	0.85	0.03	15.50	5.00
			Light off	0.98	0.02	0.19	0.06	0.89	0.03	0.93	0.03	0.27	0.05	0.83	0.03	24.00	3.89

Reference

1 Miller, E. K. & Cohen, J. D. An integrative theory of prefrontal cortex function. *Annu Rev Neurosci* **24**, 167-202 (2001). https://doi.org:DOI 10.1146/annurev.neuro.24.1.167

2 Uddin, L. Q. Cognitive and behavioural flexibility: neural mechanisms and clinical considerations. *Nat Rev Neurosci* **22**, 167-179 (2021). https://doi.org:10.1038/s41583-021-00428-w

3 Thorpe, S. J., Rolls, E. T. & Maddison, S. The orbitofrontal cortex: neuronal activity in the behaving monkey. *Exp Brain Res* **49**, 93-115 (1983). https://doi.org:10.1007/BF00235545

4 Hornak, J. *et al.* Reward-related reversal learning after surgical excisions in orbito-frontal or dorsolateral prefrontal cortex in humans. *J Cogn Neurosci* **16**, 463-478 (2004). https://doi.org:10.1162/089892904322926791

5 Kim, C., Johnson, N. F., Cilles, S. E. & Gold, B. T. Common and distinct mechanisms of cognitive flexibility in prefrontal cortex. *J Neurosci* **31**, 4771-4779 (2011). https://doi.org:10.1523/JNEUROSCI.5923-10.2011

6 Cole, M. W. *et al.* Multi-task connectivity reveals flexible hubs for adaptive task control. *Nat Neurosci* **16**, 1348-1355 (2013). https://doi.org:10.1038/nn.3470

7 Nee, D. E. Integrative frontal-parietal dynamics supporting cognitive control. *Elife* **10** (2021). https://doi.org:10.7554/eLife.57244

8 Okazawa, G. & Kiani, R. Neural Mechanisms That Make Perceptual Decisions Flexible. *Annu Rev Physiol* **85**, 191-215 (2023). https://doi.org:10.1146/annurev-physiol-031722-024731

9 Guo, L., Ponvert, N. D. & Jaramillo, S. The role of sensory cortex in behavioral flexibility. *Neuroscience* **345**, 3-11 (2017). https://doi.org:10.1016/j.neuroscience.2016.03.067

10 Poort, J. *et al.* Learning Enhances Sensory and Multiple Non-sensory Representations in Primary Visual Cortex. *Neuron* **86**, 1478-1490 (2015). https://doi.org:10.1016/j.neuron.2015.05.037

11 Chereau, R. *et al.* Dynamic perceptual feature selectivity in primary somatosensory cortex upon reversal learning. *Nat Commun* **11**, 3245 (2020). https://doi.org:10.1038/s41467-020-17005-x

12 Xin, Y. *et al.* Sensory-to-Category Transformation via Dynamic Reorganization of Ensemble Structures in Mouse Auditory Cortex. *Neuron* **103**, 909-921 e906 (2019). https://doi.org:10.1016/j.neuron.2019.06.004

13 Birman, D. & Gardner, J. L. A flexible readout mechanism of human sensory representations. *Nat Commun* **10**, 3500 (2019). https://doi.org:10.1038/s41467-019-11448-7

14 Jaramillo, S., Borges, K. & Zador, A. M. Auditory thalamus and auditory cortex are equally modulated by context during flexible categorization of sounds. *J Neurosci* **34**, 5291-5301 (2014). https://doi.org:10.1523/JNEUROSCI.4888-13.2014

15 Izquierdo, A., Brigman, J. L., Radke, A. K., Rudebeck, P. H. & Holmes, A. The neural basis of reversal learning: An updated perspective. *Neuroscience* **345**, 12-26 (2017). https://doi.org:10.1016/j.neuroscience.2016.03.021

16 Hattori, R. *et al.* Meta-reinforcement learning via orbitofrontal cortex. *Nat Neurosci* **26**, 2182-2191 (2023). https://doi.org:10.1038/s41593-023-01485-3

17 Toth, J. *et al.* Dynamic gating of perceptual flexibility by non-classically responsive cortical neurons. *Res Sq* (2024). https://doi.org:10.21203/rs.3.rs-4650869/v1

18 Banerjee, A. *et al.* Value-guided remapping of sensory cortex by lateral orbitofrontal cortex. *Nature* **585**, 245-250 (2020). https://doi.org:10.1038/s41586-020-2704-z

19 Zingg, B. *et al.* Neural networks of the mouse neocortex. *Cell* **156**, 1096-1111 (2014). https://doi.org:10.1016/j.cell.2014.02.023

20 Lewis, J. W. & Van Essen, D. C. Corticocortical connections of visual, sensorimotor, and multimodal processing areas in the parietal lobe of the macaque monkey. *J Comp Neurol* **428**, 112-137 (2000). https://doi.org:10.1002/1096-9861(20001204)428:1<112::aid-cne8>3.0.co;2-9

21 Wang, B. A., Veismann, M., Banerjee, A. & Pleger, B. Human orbitofrontal cortex signals decision outcomes to sensory cortex during behavioral adaptations. *Nat Commun* **14**, 3552 (2023). https://doi.org:10.1038/s41467-023-38671-7

22 D'Cruz, A. M., Ragozzino, M. E., Mosconi, M. W., Pavuluri, M. N. & Sweeney, J. A. Human reversal learning under conditions of certain versus uncertain outcomes. *Neuroimage* **56**, 315-322 (2011). https://doi.org:10.1016/j.neuroimage.2011.01.068

23 Pho, G. N., Goard, M. J., Woodson, J., Crawford, B. & Sur, M. Task-dependent representations of stimulus and choice in mouse parietal cortex. *Nature Communications* **9** (2018). https://doi.org:ARTN 259610.1038/s41467-018-05012-y

24 Zhong, L. *et al.* Causal contributions of parietal cortex to perceptual decision-making during stimulus

categorization. *Nat Neurosci* **22**, 963-973 (2019). https://doi.org:10.1038/s41593-019-0383-6

25 Han, S. & Helmchen, F. Behavior-relevant top-down cross-modal predictions in mouse neocortex. *Nat Neurosci* **27**, 298-308 (2024). https://doi.org:10.1038/s41593-023-01534-x

26 Akrami, A., Kopec, C. D., Diamond, M. E. & Brody, C. D. Posterior parietal cortex represents sensory history and mediates its effects on behaviour. *Nature* **554**, 368-372 (2018). https://doi.org:10.1038/nature25510

27 Hwang, E. J., Dahlen, J. E., Mukundan, M. & Komiyama, T. History-based action selection bias in posterior parietal cortex. *Nat Commun* **8**, 1242 (2017). https://doi.org:10.1038/s41467-017-01356-z

28 David, S. V., Fritz, J. B. & Shamma, S. A. Task reward structure shapes rapid receptive field plasticity in auditory cortex. *Proc Natl Acad Sci U S A* **109**, 2144-2149 (2012). https://doi.org:10.1073/pnas.1117717109

29 Yang, Y., Lee, J. & Kim, G. Integration of locomotion and auditory signals in the mouse inferior colliculus. *Elife* **9** (2020). https://doi.org:10.7554/eLife.52228

30 Rinne, T. *et al.* Auditory selective attention modulates activation of human inferior colliculus. *J Neurophysiol* **100**, 3323-3327 (2008). https://doi.org:10.1152/jn.90607.2008

31 Guo, L., Weems, J. T., Walker, W. I., Levichev, A. & Jaramillo, S. Choice-Selective Neurons in the Auditory Cortex and in Its Striatal Target Encode Reward Expectation. *J Neurosci* **39**, 3687-3697 (2019). https://doi.org:10.1523/JNEUROSCI.2585-18.2019

32 Drieu, C. *et al.* Rapid emergence of latent knowledge in the sensory cortex drives learning. *Nature* (2025). https://doi.org:10.1038/s41586-025-08730-8

33 Zempeltzi, M. M. *et al.* Task rule and choice are reflected by layer-specific processing in rodent auditory cortical microcircuits. *Commun Biol* **3**, 345 (2020). https://doi.org:10.1038/s42003-020-1073-3

34 Li, J. C. *et al.* Primary Auditory Cortex is Required for Anticipatory Motor Response. *Cereb Cortex* **27**, 3254-3271 (2017). https://doi.org:10.1093/cercor/bhx079

35 Znamenskiy, P. & Zador, A. M. Corticostriatal neurons in auditory cortex drive decisions during auditory discrimination. *Nature* **497**, 482-485 (2013). https://doi.org:10.1038/nature12077

36 Ford, A. N., Czarny, J. E., Rogalla, M. M., Quass, G. L. & Apostolides, P. F. Auditory Corticofugal Neurons Transmit Auditory and Non-auditory Information During Behavior. *J Neurosci* **44** (2024). https://doi.org:10.1523/JNEUROSCI.1190-23.2023

37 Niwa, M., Johnson, J. S., O'Connor, K. N. & Sutter, M. L. Activity Related to Perceptual Judgment and Action in Primary Auditory Cortex. *Journal of Neuroscience* **32**, 3193-3210 (2012). https://doi.org:10.1523/Jneurosci.0767-11.2012

38 Quass, G. L., Rogalla, M. M., Ford, A. N. & Apostolides, P. F. Mixed Representations of Sound and Action in the Auditory Midbrain. *Journal of Neuroscience* **44** (2024). https://doi.org:ARTN e183123202410.1523/JNEUROSCI.1831-23.2024

39 Metzger, R. R., Greene, N. T., Porter, K. K. & Groh, J. M. Effects of reward and behavioral context on neural activity in the primate inferior colliculus. *Journal of Neuroscience* **26**, 7468-7476 (2006). https://doi.org:10.1523/Jneurosci.5401-05.2006

40 Rodgers, C. C. & DeWeese, M. R. Neural Correlates of Task Switching in Prefrontal Cortex and Primary Auditory Cortex in a Novel Stimulus Selection Task for Rodents. *Neuron* **82**, 1157-1170 (2014). https://doi.org:10.1016/j.neuron.2014.04.031

41 Liu, Y. H., Xin, Y. & Xu, N. L. A cortical circuit mechanism for structural knowledge-based flexible sensorimotor decision-making. *Neuron* **109**, 2009-+ (2021). https://doi.org:10.1016/j.neuron.2021.04.014

42 Winnubst, J. *et al.* Reconstruction of 1,000 Projection Neurons Reveals New Cell Types and Organization of Long-Range Connectivity in the Mouse Brain. *Cell* **179**, 268-281 e213 (2019). https://doi.org:10.1016/j.cell.2019.07.042

43 Munoz-Castaneda, R. *et al.* Cellular anatomy of the mouse primary motor cortex. *Nature* **598**, 159-166 (2021). https://doi.org:10.1038/s41586-021-03970-w

44 Stringer, C. *et al.* Rastermap: a discovery method for neural population recordings. *Nat Neurosci* **28**, 201-212 (2025). https://doi.org:10.1038/s41593-024-01783-4

45 Pachitariu, M. *et al.* Suite2p: beyond 10,000 neurons with standard two-photon microscopy. *BioRxiv* (2016). https://doi.org:https://doi.org/10.1101/061507

46 Chudasama, Y. & Robbins, T. W. Dissociable contributions of the orbitofrontal and infralimbic cortex to pavlovian autoshaping and discrimination reversal learning: further evidence for the functional heterogeneity of the rodent frontal cortex. *J Neurosci* **23**, 8771-8780 (2003). https://doi.org:10.1523/JNEUROSCI.23-25-08771.2003

47 Kesner, R. P. & Churchwell, J. C. An analysis of rat prefrontal cortex in mediating executive function. *Neurobiol Learn Mem* **96**, 417-431 (2011). https://doi.org:10.1016/j.nlm.2011.07.002

48 Cho, S., Lee, H., Baek, S. & Paik, S.-B. Neuromimetic metaplasticity for adaptive continual learning. *arXiv preprint arXiv:2407.07133* (2024).

49 van de Ven, G. M., Soures, N. & Kudithipudi, D. Continual learning and catastrophic forgetting. *arXiv preprint arXiv:2403.05175* (2024).

50 Jarvers, C. *et al.* Reversal Learning in Humans and Gerbils: Dynamic Control Network Facilitates Learning. *Front Neurosci* **10**, 535 (2016). https://doi.org:10.3389/fnins.2016.00535

51 Gabriel, M., Orona, E., Foster, K. & Lambert, R. W. Cingulate cortical and anterior thalamic neuronal correlates of reversal learning in rabbits. *J Comp Physiol Psychol* **94**, 1087-1100 (1980). https://doi.org:10.1037/h0077739

52 Gonzalez, R. C., Behrend, E. R. & Bitterman, M. E. Reversal learning and forgetting in bird and fish. *Science* **158**, 519-521 (1967). https://doi.org:10.1126/science.158.3800.519

53 Gossette, R. L. Analysis of Reversal and Non-Reversal Training: Further Examination of the Retention Decrement Hypothesis. *Perceptual and Motor Skills* **29**, 171-178 (1969). https://doi.org:10.2466/pms.1969.29.1.171

54 Du, X. *et al.* The multifaceted role of the inferior colliculus in sensory prediction, reward processing, and decision-making. *Elife* **13** (2025). https://doi.org:10.7554/eLife.101142

55 Asilador, A. & Llano, D. A. Top-Down Inference in the Auditory System: Potential Roles for Corticofugal Projections. *Front Neural Circuits* **14**, 615259 (2020). https://doi.org:10.3389/fncir.2020.615259

56 Kraus, N. Descending Control in the Auditory System: A Perspective. *Front Neurosci* **15**, 769192 (2021). https://doi.org:10.3389/fnins.2021.769192

57 Lee, T.-Y., Weissenberger, Y., King, A. J. & Dahmen, J. C. (eLife Sciences Publications, Ltd, 2024).

58 Gulati, S., Cao, V. Y. & Otte, S. Multi-layer Cortical Ca2+ Imaging in Freely Moving Mice with Prism Probes and Miniaturized Fluorescence Microscopy. *J Vis Exp* (2017). https://doi.org:10.3791/55579

59 Jeong, H., Kim, D., Song, M., Paik, S. B. & Jung, M. W. Distinct roles of parvalbumin- and somatostatin-expressing neurons in flexible representation of task variables in the prefrontal cortex. *Prog Neurobiol* **187**, 101773 (2020). https://doi.org:10.1016/j.pneurobio.2020.101773

60 Pachitariu, M., Sridhar, S., Pennington, J. & Stringer, C. Spike sorting with Kilosort4. *Nat Methods* **21**, 914-921 (2024). https://doi.org:10.1038/s41592-024-02232-7

61 Raposo, D., Kaufman, M. T. & Churchland, A. K. A category-free neural population supports evolving demands during decision-making. *Nat Neurosci* **17**, 1784-1792 (2014). https://doi.org:10.1038/nn.3865

62 Ghosh, K. K. *et al.* Miniaturized integration of a fluorescence microscope. *Nat Methods* **8**, 871-878 (2011). https://doi.org:10.1038/nmeth.1694

63 Ziv, Y. *et al.* Long-term dynamics of CA1 hippocampal place codes. *Nat Neurosci* **16**, 264-266 (2013). https://doi.org:10.1038/nn.3329

64 Pinto, L. & Dan, Y. Cell-Type-Specific Activity in Prefrontal Cortex during Goal-Directed Behavior. *Neuron* **87**, 437-450 (2015). https://doi.org:10.1016/j.neuron.2015.06.021

65 Bondanelli, G., Deneux, T., Bathellier, B. & Ostojic, S. Network dynamics underlying OFF responses in the auditory cortex. *Elife* **10** (2021). https://doi.org:10.7554/eLife.53151

66 Knyazev, A. V. & Argentati, M. E. Principal angles between subspaces in an-based scalar product:: Algorithms and perturbation estimates. *Siam J Sci Comput* **23**, 2008-2040 (2002). https://doi.org:Pii S1064827500377332Doi 10.1137/S1064827500377332

67 Miri, A., Daie, K., Burdine, R. D., Aksay, E. & Tank, D. W. Regression-Based Identification of Behavior-Encoding Neurons During Large-Scale Optical Imaging of Neural Activity at Cellular Resolution. *Journal of Neurophysiology* **105**, 964-980 (2011). https://doi.org:10.1152/jn.00702.2010

68 Chen, J. L., Voigt, F. F., Javadzadeh, M., Krueppel, R. & Helmchen, F. Long-range population dynamics of anatomically defined neocortical networks. *Elife* **5** (2016). https://doi.org:10.7554/eLife.14679

69 Chen, T. W. *et al.* Ultrasensitive fluorescent proteins for imaging neuronal activity. *Nature* **499**, 295-300 (2013). https://doi.org:10.1038/nature12354

70 Yang, S. H. *et al.* Neural mechanism of acute stress regulation by trace aminergic signalling in the lateral habenula in male mice. *Nat Commun* **14**, 2435 (2023). https://doi.org:10.1038/s41467-023-38180-7

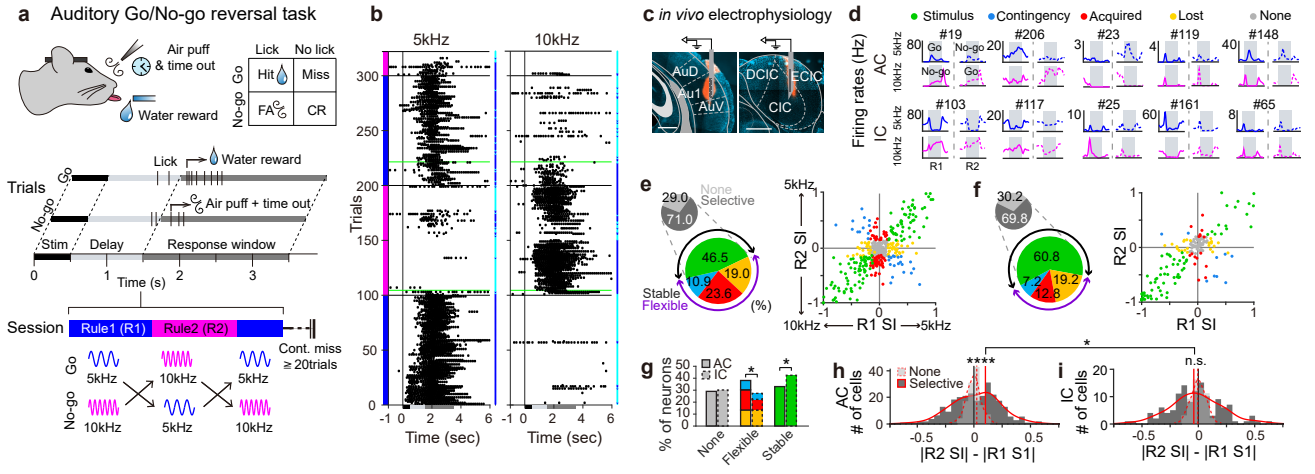
a
Auditory Go/No-go reversal task
Air puff & time out
Water reward
Lick
No lick
Go
No-go
Hit
Miss
FA
CR
Trials
Lick
Water reward
Air puff + time out
Stim
Delay
Response window
Time (s)
Session
Rule1 (R1)
Rule2 (R2)
Cont. miss ≥ 20trials
5kHz
10kHz
b
5kHz
10kHz
Trials
Time (sec)
c in vivo electrophysiology
AuD
Au1
AuV
DCIC
ECIC
CIC
d
Stimulus
Contingency
Acquired
Lost
None
Firing rates (Hz)
AC
IC
#19
#206
#23
#119
#148
#103
#117
#25
#161
#65
R1
R2
e
29.0
71.0
None
Selective
46.5
19.0
10.9
23.6
Stable
Flexible
(%)
R2 SI
R1 SI
10kHz
5kHz
f
30.2
69.8
60.8
19.2
7.2
12.8
g
% of neurons
AC
IC
None
Flexible
Stable
h
AC
# of cells
None
Selective
****
|R2 SI| - |R1 S1|
i
IC
# of cells
n.s.
*

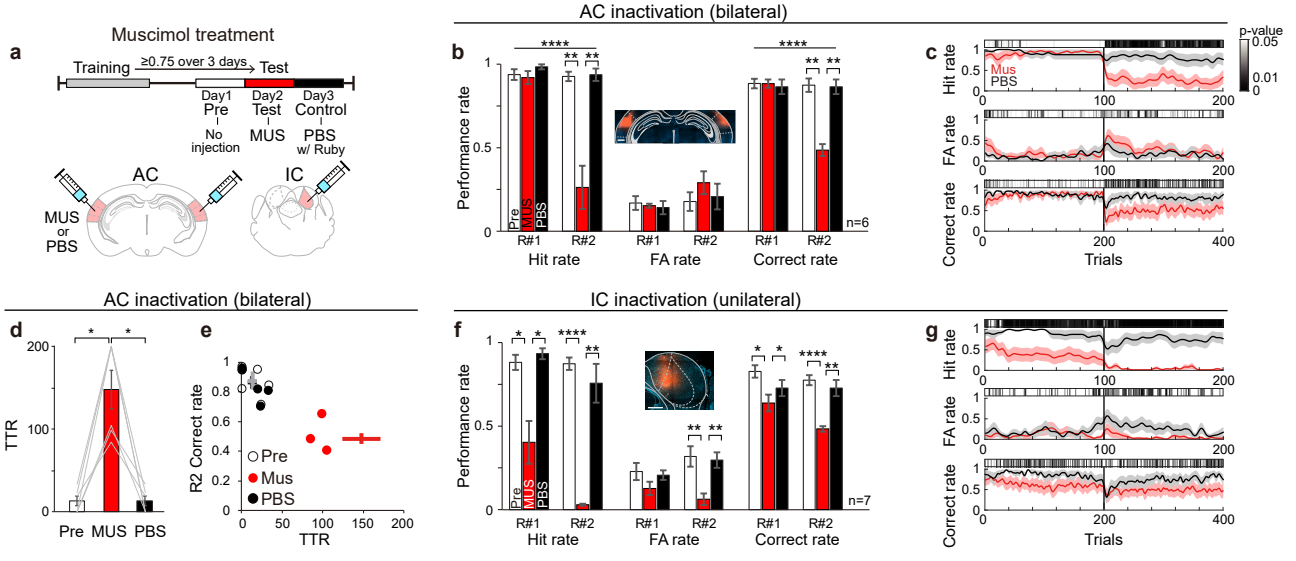
a
Muscimol treatment
Training
≥0.75 over 3 days
Test
Day1
Pre
No injection
Day2
Test
MUS
Day3
Control
PBS
w/ Ruby
AC
IC
MUS or PBS
AC inactivation (bilateral)
b
Performance rate
Pre
MUS
PBS
n=6
R#1
R#2
Hit rate
FA rate
Correct rate
c
p-value
0.05
0.01
0
Hit rate
FA rate
Correct rate
Mus
PBS
Trials
AC inactivation (bilateral)
d
TTR
Pre
MUS
PBS
e
R2 Correct rate
Pre
Mus
PBS
TTR
IC inactivation (unilateral)
f
Performance rate
n=7
g

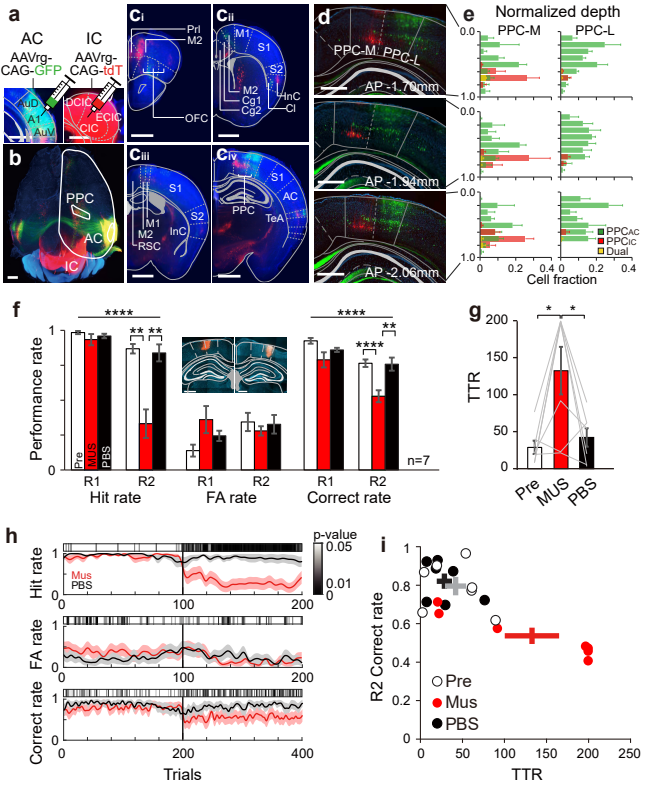
a
AC
IC
AAVrg-CAG-GFP
AAVrg-CAG-tdT
AuD
A1
AuV
PCIc
ECIc
CIC
Ci
Prl
M2
OFC
Cii
M1
S1
S2
M2
Cg1
Cg2
InC
CI
b
PPC
AC
IC
Ciii
S1
S2
M1
M2
RSC
InC
Civ
S1
AC
PPC
TeA
d
PPC-M
PPC-L
AP -1.70mm
AP -1.94mm
AP -2.06mm
e
Normalized depth
PPC-M
PPC-L
0.0
1.0
PPCAC
PPCIc
Dual
0
0.2
0.4
Cell fraction
f
****
**
Performance rate
1
0
Pre
MUS
PBS
R1
R2
Hit rate
FA rate
Correct rate
n=7
g
*
TTR
200
150
100
50
0
Pre
MUS
PBS
h
Hit rate
FA rate
Correct rate
Mus
PBS
p-value
0.05
0.01
0
100
200
400
Trials
i
R2 Correct rate
TTR
Pre
Mus
PBS
0
50
100
150
200
250

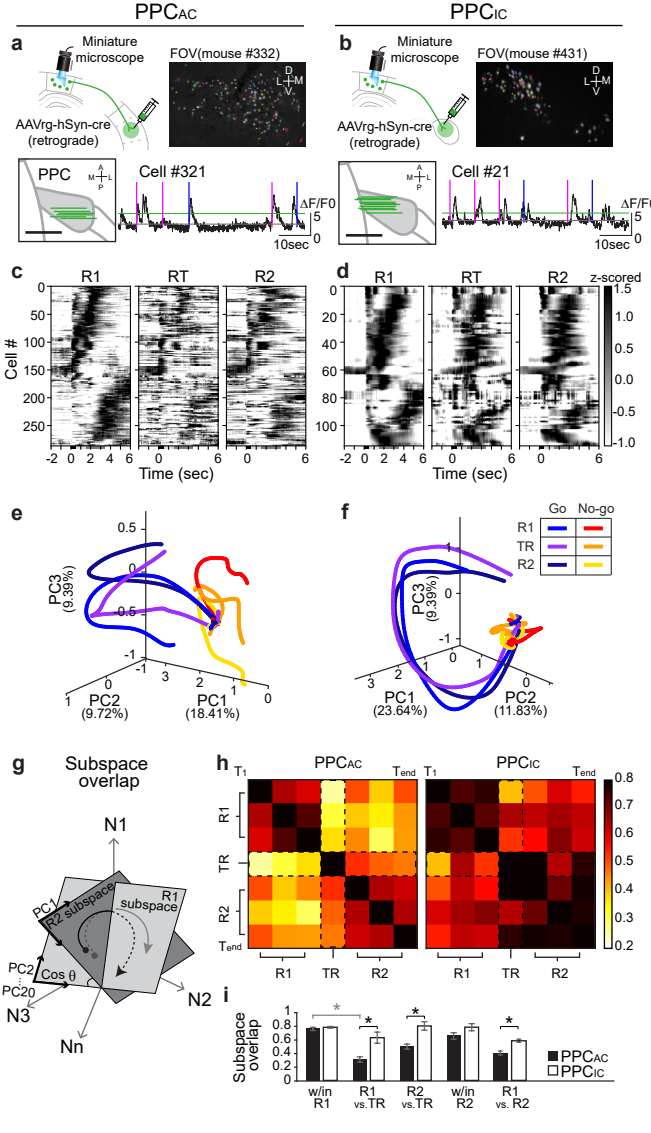
PPCAC
PPCIC
a
Miniature microscope
AAVrg-hSyn-cre (retrograde)
FOV(mouse #332)
D
L
M
V
PPC
A
M
L
P
Cell #321
ΔF/F0
5
0
10sec
b
Miniature microscope
AAVrg-hSyn-cre (retrograde)
FOV(mouse #431)
Cell #21
c
R1
RT
R2
Cell #
Time (sec)
d
z-scored
e
PC3 (9.39%)
PC2 (9.72%)
PC1 (18.41%)
f
Go
No-go
R1
TR
R2
PC1 (23.64%)
PC2 (11.83%)
g
Subspace overlap
N1
N2
N3
Nn
PC1
PC2
PC20
R2 subspace
R1 subspace
Cos θ
h
PPCAC
PPCIC
T1
Tend
R1
TR
R2
i
Subspace overlap
w/in R1
R1 vs.TR
R2 vs.TR
w/in R2
R1 vs. R2
PPCAC
PPCIC

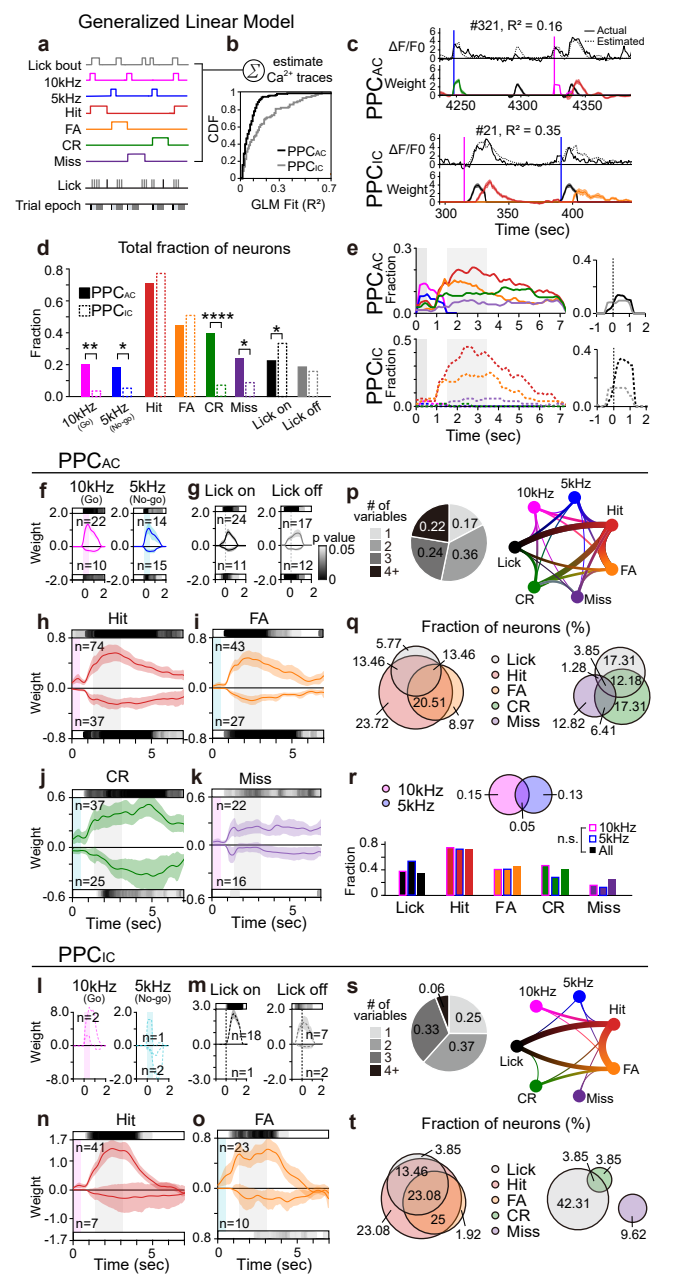
Generalized Linear Model
a
Lick bout
10kHz
5kHz
Hit
FA
CR
Miss
Lick
Trial epoch
b
estimate Ca2+ traces
CDF
GLM Fit (R2)
PPCAC
PPCIC
c
#321, R2 = 0.16
Actual
Estimated
ΔF/F0
Weight
PPCAC
#21, R2 = 0.35
PPCIC
Time (sec)
d
Total fraction of neurons
Fraction
10kHz (Go)
5kHz (No-go)
Hit
FA
CR
Miss
Lick on
Lick off
e
PPCAC Fraction
PPCIC Fraction
Time (sec)
PPCAC
f
10kHz (Go)
5kHz (No-go)
Weight
g
Lick on
Lick off
p value
p
# of variables
1
2
3
4+
Lick
10kHz
5kHz
Hit
FA
CR
Miss
h
Hit
i
FA
q
Fraction of neurons (%)
Lick
Hit
FA
CR
Miss
j
CR
k
Miss
Time (sec)
r
10kHz
5kHz
n.s.
All
Fraction
Lick
Hit
FA
CR
Miss
PPCIC
l
10kHz (Go)
5kHz (No-go)
m
Lick on
Lick off
s
# of variables
n
Hit
o
FA
Time (sec)
t
Fraction of neurons (%)
Lick
Hit
FA
CR
Miss

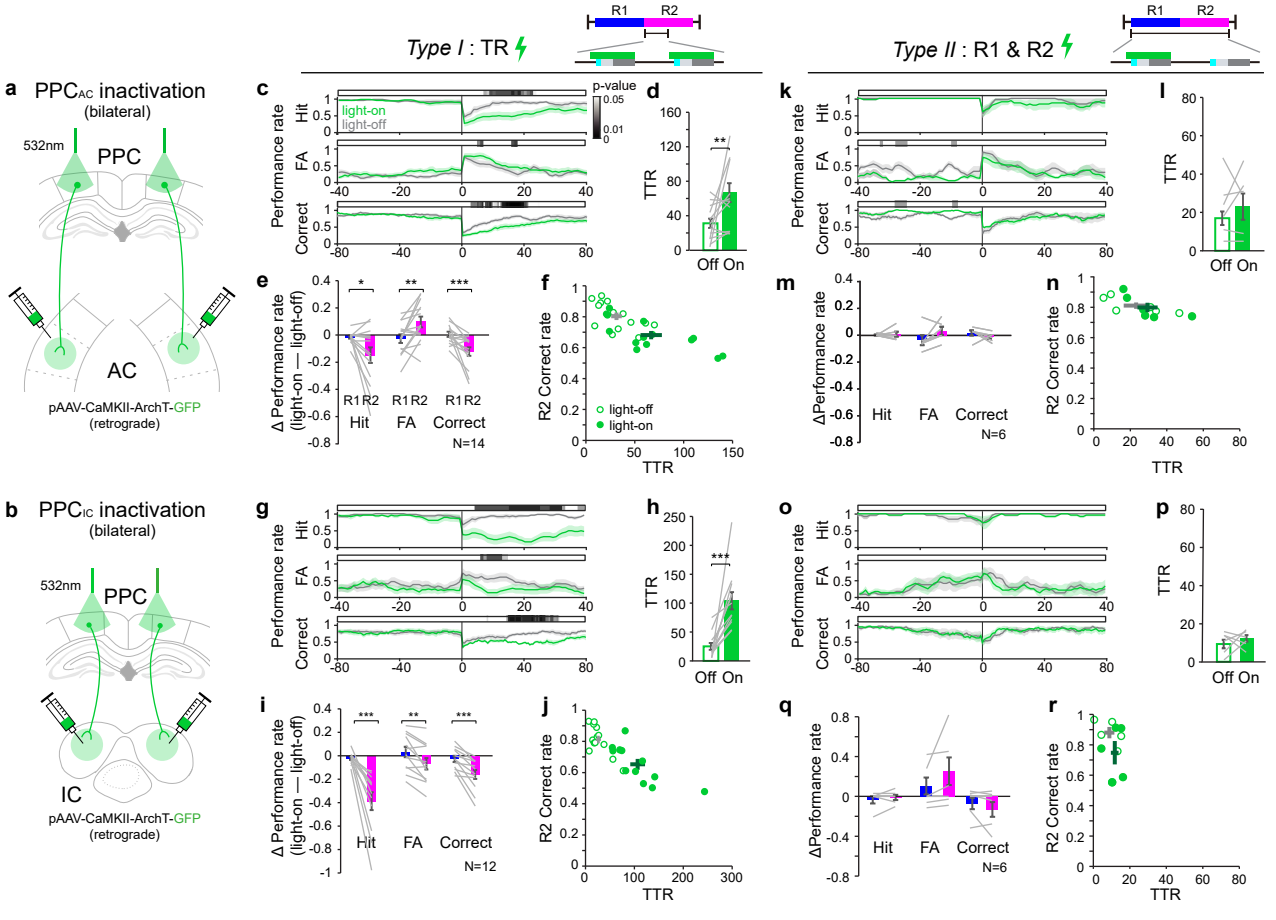
Type I : TR
Type II : R1 & R2
R1
R2
a PPCAC inactivation
(bilateral)
532nm
PPC
AC
pAAV-CaMKII-ArchT-GFP
(retrograde)
b PPCIC inactivation
(bilateral)
IC
c
d
e
f
g
h
i
j
k
l
m
n
o
p
q
r
Performance rate
Hit
FA
Correct
light-on
light-off
p-value
0.05
0.01
0
TTR
Off On
Δ Performance rate
(light-on — light-off)
ΔPerformance rate
R2 Correct rate
N=14
N=12
N=6